University of Alberta

Response of Lipid Olefinic Protons to *In-Vivo* Magnetic Resonance Spectroscopy Sequences at 3 T

by

Ayhan Bingölbali

A thesis submitted to the Faculty of Graduate Studies and Research
in partial fulfillment of the requirements for the degree of

Master of Science

in

Medical Physics

Department of Oncology

Spring 2014
Edmonton, Alberta

Abstract

Magnetic Resonance Spectroscopy (MRS) measurements of lipid unsaturation are relevant in the study of a number of diseases. The olefinic resonance yields a measure of lipid unsaturation and is often obscured by water signal *in-vivo*. The objective of this work is to investigate the response of lipid olefinic protons to STEAM, one of two standard *in-vivo* MRS methods (the other being PRESS). STEAM timing parameters were chosen (mixing time = 20 ms, echo time = 100 ms) to sufficiently resolve the olefinic resonance from that of water *in-vivo* while ensuring that it did not suffer significant signal losses due to J-coupling. The optimized STEAM sequence was employed to acquire signal from spinal bone marrow of four volunteers, and on average it provided 91% more olefinic signal (by area) compared to the signal acquired with a previously optimized PRESS sequence at 3 T.

Acknowledgements

After having a Ph.D. degree, the medical physics master program was a quite challenging step in the journey of my life. I received the generous support, contribution, and motivation by many people to successfully complete the journey of my master thesis. Now I would like to take the opportunity to acknowledge and thank all of them.

First of all, I would like to gratefully thank my master thesis' supervisor, Dr. Atiyah Yahya, for her valuable time, guidance, contribution, and support. She reviewed all drafts of the thesis, and provided critical comments and corrections. She was always there whenever I needed help during this study. I am indebted to Dr. Yahya for her enormous contribution and I feel privileged to have been working with her.

I would also like to gratefully thank my master thesis supervisory committee members Dr. B. Gino Fallone, Dr. Nicola De Zanche, and Dr. Hans-Sonke Jans, for their valuable time, great suggestions, crucial comments and corrections on my thesis.

I would also like gratefully thank Dr. Alan H. Wilman, who was my arms' length examiner on the thesis defense, for his critical comments and corrections on my thesis.

I would also like to thank Dr. Brad Warkentin, the chair of my thesis defense, for his valuable time on my thesis defense.

I am also thankful to all academic and administrative staffs of the Department of Medical Physics and Oncology, including all graduate students, Mr. Dan Michael Santos, and all MRI volunteers of this study for their camaraderie and support.

I am also really thankful to my friend, Dr. Amir Keyvanloo for his valuable time and support.

I would also like to gratefully thank Dr. Andrew Shaw and Mr. Dan Fredrick for their valuable time and support, which was tremendously helpful.

I would also like to thank Yildiz Technical University for giving me the chance to study this program.

Funding for this program was provided by the Antoine Noujaim Graduate Entrance Scholarship, the Natural Sciences and Engineering Research Council of Canada (NSERC), and Canadian Breast Cancer Foundation (CBCF) - Prairies/NWT Region. I am grateful for the funds and thank for their generous supports. I would also like to thank the Medical Physics Department and Cross Cancer Institute for providing necessary facilities for my studies.

Last, but by no means the least, I am always gratefully to all of my family members, especially my wife, Dr. Nurcan Bingölbali, for their constant love, prayers, and support that motivate me to deal with any difficulties.

Table of Contents

List of Figures

List of Tables

List of Abbreviations

BW_{rf}	Bandwidth of RF pulse
DHA	Docosahexaenoic acid
DPA	Docosapentaenoic acid
TE	Echo time
EPA	Eicosapentaenoic acid
EMF	Electromagnetic force
FA	Fatty acid
FOV	Field of view
FT	Fourier transform
FID	Free induction decay
MRI	Magnetic resonance imaging
MRS	Magnetic resonance spectroscopy
TM	Mixing time
MUFA	Monounsaturated fatty acid
NMR	Nuclear magnetic resonance
NSA	Number of signal averages
PRESS	Point resolved spectroscopy
PUFA	Polyunsaturated fatty acid
^{1}H	Proton
RF	Radiofrequency
TR	Repetition time
SFA	Saturated fatty acid
Sel-MQC	Selective multiple-quantum coherence transfer
SNR	Signal to noise ratio
SE	Spin echo
STEAM	Stimulated echo acquisition mode
TMS	Tetramethylsilane
UFA	Unsaturated fatty acid
VOI	Volume of interest

Chapter 1 Introduction

1.1 Introduction to Thesis

Nuclear Magnetic Resonance (NMR), which is a non-destructive and non-invasive method, provides information about the metabolism of cells, tissues, organs, and fat composition of living systems[1,2]. Proton (^{1}H) magnetic resonance spectroscopy (MRS) provides a means of non-invasive biochemical analysis and has been applied *in-vivo* to study a number of different diseases and disorders. Proton MRS measurements of lipids have been made to better understand obesity[3,4,5], diabetes[3,6,7] , liver disease[8,9] and cancer[3,10,11,12]. Recently, efforts have been made to measure levels of lipid unsaturation (amount of carbon-carbon double bonds) *in-vivo* by proton MRS. Such measurements have been made in liver[13,14], adipose tissue[2,15,16,17], breast tissue[18,19,20] and marrow fat[21,22]. It was found that unsaturation levels were lower in cancerous breast tissue compared to healthy breast tissue[18]; lower levels of lipis unsaturation were also found in metastatic axillary lymph nodes[20]. Levels of lipid unsaturation are estimated based on the olefinic resonance which resonates at about 5.35 ppm and which arises from the protons bonded to the double bonded carbons. However, observing the olefinic resonance *in-vivo* is challenging at clinical field strengths, such as 1.5 and 3 T, because it is often largely obscured by the water peak which has a large peak at about 4.75 ppm making standard *in-vivo* MRS pulse sequences such as short echo time (TE) Point Resolved Spectroscopy (PRESS) and Stimulated Echo Acquisition Mode (STEAM) not suitable for its quantification. The TE is a timing parameter of the sequences. Water suppression techniques are likely to affect the olefinic resonance[13] and therefore previously PRESS has been optimized for observing the olefinic resonance *in-vivo* by using a long-TE which resolves the olefinic peak from that of water[13,22]. The water signal decays

due to transverse (T_2) relaxation (a dephasing of the signal) at a faster rate than the olefinic protons do enabling the observation of a well resolved olefinic peak. However, caution was employed in the choice of TE; it is essential that the TE is not one at which the olefinic signal suffers significant losses due to J-coupling interactions. J-coupling interactions (which are exhibited by the olefinic protons but not water protons) cause the signal intensity and lineshape of the coupled spins to be dependent on the TE of the pulse sequence. Previously, a PRESS sequence with a long TE of 200 ms was found to be suitable for olefinic signal measurement in liver at 1.5 T[13]. PRESS was also recently optimized for measuring the olefinic resonance at 3 T in spinal bone marrow by employing a TE of 200 ms[22], at which the olefinic protons exhibited minimal J-coupling losses. However, a TE of 200 ms is relatively long and likely results in significant T_2 signal loss *in-vivo* for the olefinic protons themselves. Signal to noise ratio (SNR) is of high importance in MRS. Increasing the SNR requires an increase in the number of signal averages (SNR ≈ √(number of averages)), and hence an increase in scan time. Any improvement in SNR provides the advantage of reducing the acquisition time which is of particular relevance when scanning within a time frame that the patient can tolerate.

The work of this thesis examines the response of lipid olefinic protons to a standard STEAM pulse sequence at 3 T. We investigate whether a shorter TE (less than 200 ms) can be determined at which: a) the olefinic protons do not suffer significant losses due to J-coupling evolution, b) the olefinic resonance is well resolved from water *in vivo* and c) the olefinic signal provided by the STEAM sequence *in-vivo* is higher than that provided by the previously optimized PRESS sequence at 3 T. To our knowledge the response of the olefinic protons to long-TE STEAM has not been previously investigated. Experiments were conducted on nine edible oils and on spinal bone marrow *in-vivo*.

Chapter 1 of this thesis provides the basic principles of MRS, including explanations of the concepts of chemical shift, scalar coupling, relaxation, and the response of a simple coupled spin system to PRESS and STEAM. Chapter 2 gives an overview of fatty acids, their characteristic NMR spectra, oil compositions, and the methods employed for *in-vitro* and *in-vivo* scans and for the data analysis. Chapter 3 provides the outcomes of the investigations. The long-TE STEAM sequence was optimized by examining the response of the olefinic protons of nine edible oils to a standard STEAM sequence as a function of its timing parameters. The outcome of applying the optimal STEAM timings *in-vivo* to the spinal bone marrow of four healthy volunteers was compared to that obtained by applying the previously optimized PRESS sequence in spinal bone marrow. Chapter 4 offers concluding remarks to the thesis.

1.2 Nuclear Magnetic Moments

To be NMR viable, a nucleus must have a nuclear magnetic moment, $\vec{\mu}$. Nuclei are formed of protons and neutrons. A proton has positive charge (+1) while a neutron has no net charge. The sum of the number of protons (also known as the atomic number, Z) and the number of neutrons, N, yields the atomic mass number, A, of an atom (A = Z + N). The nucleus possesses a magnetic moment if the number of either or both of protons and neutrons is odd.

1.3 Principles of Nuclear Magnetic Resonance (NMR)

The angular momentum of an atomic nucleus, $\vec{P}$, is related to the spin quantum number (also known the spin of the nucleus), I by $\vec{P}=\hbar\vec{I}$, where $\hbar=\frac{h}{2\pi}$, h is the Plank's constant ($6.63\text{x}10^{-34}$ J s). The magnitude of P is given by[23]

$$P=\hbar\sqrt{I(I+1)}. \qquad 1.1$$

The spin quantum number, *I*, can only be integral or half-integral according to the following rules[1,24]:

i) $I = 0$ for nuclei with even numbers of both protons and neutrons (e.g., ^{12}C, ^{16}O, ^{32}S) because the internal circulating currents cancel each other.

ii) Half integral values $I = 1/2, 3/2, 5/2,..., 9/2$ for nuclei with odd mass numbers (e.g., ^{1}H, ^{13}C, ^{15}N, ^{23}Na, ^{31}P).

iii) Integral values $I = 1, 2,...$ for nuclei with even mass numbers (e.g., ^{2}H, ^{14}N) and odd number of neutrons.

The direction of angular momentum is specified by a second quantum number. The component of angular momentum along the z-direction, P_z, is given by

$$P_z = m\hbar, \qquad 1.2$$

where *m* is restricted to the discrete values $I, I-1, I-2, ...-I$ for a given value of I [23]. For example, for the spin quantum number $I = \frac{1}{2}$, $m = \frac{1}{2}$ or $m = -\frac{1}{2}$, and thus $P_z = \pm\frac{1}{2}\hbar$ [1].

The relation between a magnetic moment, $\vec{\mu}$, and the angular momentum, $\vec{P}$, is given as[24],

$$\vec{\mu} = \gamma\vec{P}, \qquad 1.3$$

where γ is the gyromagnetic ratio of the nucleus. The magnetic moment will also be quantized due to the quantized angular momentum. Equ.(1.3) can be rewritten easily for the component of the magnetic moment along the z-axis with using Equ. (1.2),

$$\mu_z = \gamma\hbar m. \qquad 1.4$$

The interaction energy between an externally applied magnetic field, $\overrightarrow{B_o}$ along the z-direction and the magnetic moment is given by

$$E = -\vec{\mu}\cdot\vec{B}_o = -(\mu_x,\mu_y,\mu_z).(0,0,B_o) = -\mu_z B_o = -\gamma\hbar m B_o = \pm\frac{\gamma\hbar B_o}{2}. \qquad 1.5$$

The two energy states are related to spins being parallel and anti-parallel to B_o, as shown in Figure 1.1(a). The lower energy level called the $|\alpha\rangle$ state has spin 1/2 and is parallel to B_o, while the upper energy level is called $|\beta\rangle$ state with spin -1/2 and is anti-parallel to B_o, as shown in Figure 1.2. The energy difference, ΔE, (known as the Zeeman energy) between the two states is given by

$$\Delta E = E_{|\beta\rangle} - E_{|\alpha\rangle} = \gamma\hbar B_o. \qquad 1.6$$

The net magnetization, $\overrightarrow{M_o}$, is equal to $\frac{\gamma\hbar}{2}(N_{|\alpha\rangle} - N_{|\beta\rangle})$, where $N_{|\alpha\rangle}$ is the number of spins parallel to B_o and $N_{|\beta\rangle}$ is the number of anti-parallel spins. If a radiofrequency (RF) field, B_1, (also known as an oscillating magnetic field) is applied perpendicular to M_o with a frequency (in the x-y plane shown in Figure 1.1b) ν_o, transitions between the two energy states take place, and a resonance condition occurs[1,24]. The magnetic energy given by Equ.(1.6) equals the energy of the electromagnetic wave[23]

$$\Delta E = h\nu_o. \qquad 1.7$$

The Larmor equation can be obtained (the resonance condition) from Equ.(1.6), and (1.7),

$$2\pi\nu_o = \omega_o = \gamma B_o, \qquad 1.8$$

where ω_o is the Larmor frequency of the nuclei.

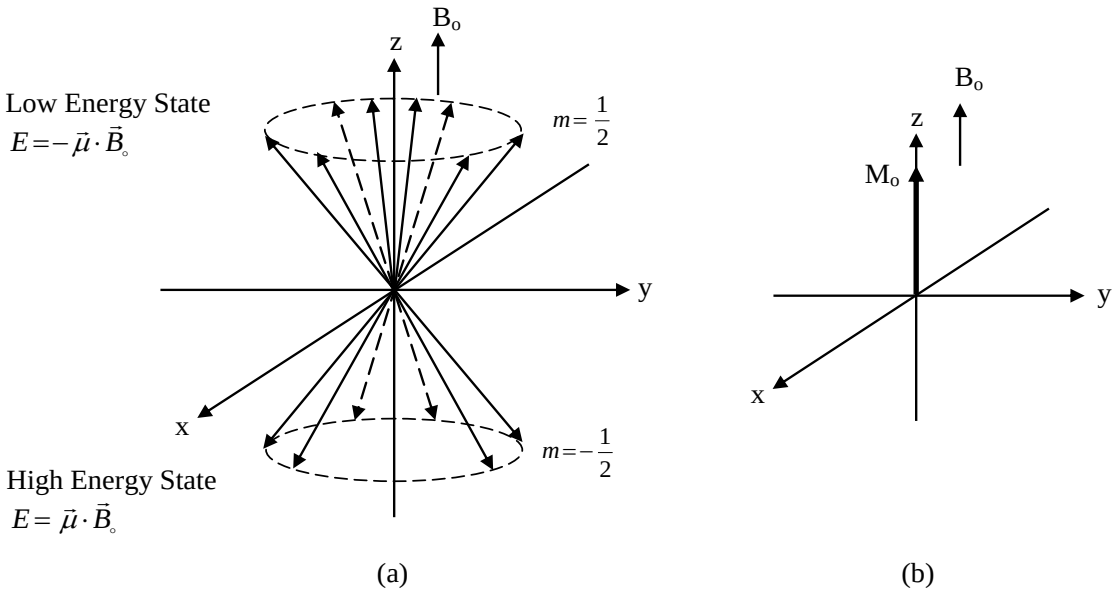

Figure 1.1. (a) The two possibility of spin states for nuclei of spin $I = \frac{1}{2}$ ($m = \frac{1}{2}$ or $m = -\frac{1}{2}$), as parallel (low energy state) and anti-parallel (high energy state) to a uniform, static magnetic field B_o applied along the z-direction. The magnetic moment vectors precess about B_o , and give two cones. (b) The net spin magnetization vector, M_o, is equal to the net z component of the magnetic moments.

1.3.1 The Populations of the Nuclear Spin States

Figure 1.2 shows the two possibility of spin states for nuclei of spin $I=\frac{1}{2}$. The parallel

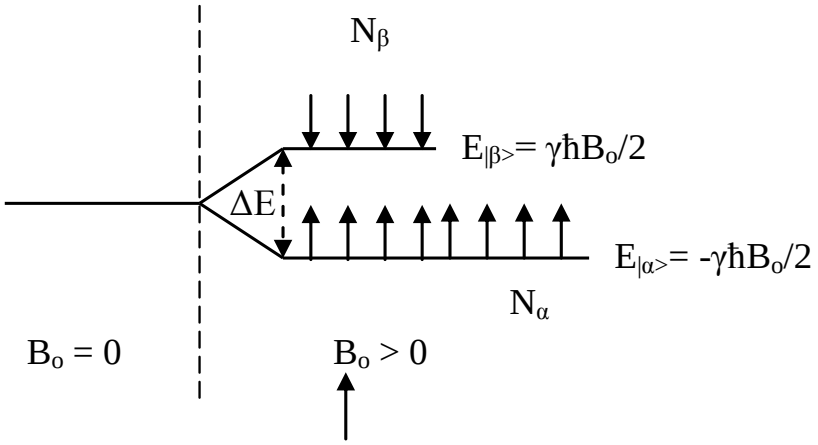

Figure 1.2. For a nucleus of spin $I=\frac{1}{2}$, only two energy levels exist. The lower energy level called $|\alpha\rangle$ state with spin 1/2 is parallel to B_o, and the upper energy level called $|\beta\rangle$ state with spin -1/2 is anti-parallel to B_o when $B_o > 0$. The energy difference between the two states is $\gamma\hbar B_o$. More spins are aligned along $\overrightarrow{B_o}$.

orientation has a lower energy compared to the anti-parallel one and therefore the parallel state is slightly more populated. The population difference is determined by the Boltzmann distribution[24],

$$\frac{N_{|\alpha\rangle}}{N_{|\beta\rangle}}=\exp\left(\frac{\Delta E}{kT}\right)=\exp\left(\frac{\gamma\hbar B_o}{kT}\right), \qquad 1.9$$

where $N_{|\alpha\rangle}$ is the number of spins in the $|\alpha\rangle$ state, $N_{|\beta\rangle}$ is the number of spins in the $|\beta\rangle$ state, k is the Boltzmann constant (1.381 x 10^{-23}J/K) and T is the temperature (in Kelvin). If kT is much larger than $\gamma\hbar B_o$, Equ.(1.9) can be approximated as[24]

$$\frac{N_{|\alpha\rangle}}{N_{|\beta\rangle}}=1+\frac{\gamma\hbar B_o}{kT}. \qquad 1.10$$

At T = 300 ^{o}K for B_o = 1 T, $\frac{N_{|\alpha\rangle} - N_{|\beta\rangle}}{N_{|\alpha\rangle} + N_{|\beta\rangle}} = 3\times10^{-6}$. Only 3 in a million protons are responsible for the NMR signal. Therefore, NMR is not a sensitive technique.

As shown in Figure 1.1a and Figure 1.2, more spins are aligned in the magnetic field direction (in the z-axis). The net spin magnetization vector, M_o, is equal to the total parallel μ vector minus the total anti-parallel μ vector, i.e. $\vec{M}_o = \sum \vec{\mu}$. In addition, the magnitude of M_o can be derived from the spin population difference at thermal equilibrium, and is given by[24]

$$M_o = \gamma^2 \hbar^2 \frac{N_{|\alpha\rangle} + N_{|\beta\rangle}}{4kT} B_o. \qquad 1.11$$

The equation indicates that the sensitivity of NMR experiments depends on several parameters besides many other factors, such as a sample volume. The hydrogen nucleus (also referred to as proton, ^{1}H) is the most commonly used nucleus due to its high natural abundance and high sensitivity. Since only ^{1}H is employed at 3 Tesla in this study, NMR properties of the ^{1}H nucleus are given in Table 1.1[1,24].

Table 1.1. ^{1}H NMR properties at 3 T.[1,24]

Nucleus	I	γ (10^6 rads^{-1}T^{-1})	Resonance frequency at 3 T (MHz)	Natural abundance (%)
^{1}H	1/2	267.52	127.8	99.985

1.3.2 The NMR Experiment

Figure 1.3 shows excitation of magnetization in the rotating frame (usually z_ρ, x_ρ, y_ρ notation is used for its axes). The rotating frame is a frame of reference that rotates at the frequency of the applied $B_1(t)$ RF. $B_1(t)$ is needed to generate the transverse magnetization, M_{xy}, to measure the NMR signal. The time varying magnetic field, $B_1(t)$, is produced by a RF coil. In

other words, the RF coil creates the time varying magnetic field ($B_1(t)$) to excite the nuclei (to generate the M_{xy}). In addition, the RF coil detects the NMR FID (Free Induction Decay) signal. Then, the Fourier Transform (FT) of the FID yields the NMR frequency-based spectrum as shown in Figure 1.3.

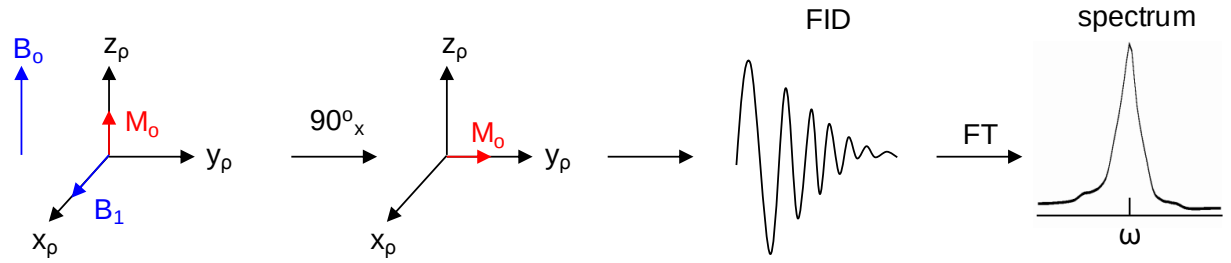

Figure 1.3. To flip M_o into the transverse plane a 90° *RF* pulse must be applied. A 90° B_1 RF pulse applied along x_ρ of the rotation frame will flip M_o onto the y_ρ axis. M_o will then precess around B_1 inducing an EMF (electromagnetic force in the surrounding RF coil). The EMF or FID signal will decay due to transverse relaxation. A Fourier Transform (FT) of the FID yields the NMR spectrum. ω is the difference between the resonance frequency of the nuclei and the rotating frame.

1.4 Chemical Shift

The power of NMR arises from the chemical shift phenomenon, where nuclei in different electronic environments resonate at different frequencies. The resonance frequency depends on the molecular environment of the nucleus[25,26]. Once the static magnetic field, B_o, is applied to a molecule, electron surrounding the nucleus precess due to the applied magnetic field. The precession creates an electronic current, which induces a small magnetic field in a direction opposite to B_o according to the Lenz's law. The effective magnetic field B_{eff} at the nucleus is given by[1,24]

$$B_{eff} = B_o - B_{o\sigma} = B_o(1-\sigma), \qquad 1.12$$

where σ is a dimensionless shielding or screening constant due to the contribution of the small induced magnetic field, $B_{o\sigma}$, generated by the electrons, and σ depends on the electronic or chemical environment of the nuclei. The outcome is that nuclei in different chemical environments have peaks at different resonance frequencies due to the different magnetic fields that they experience. This can be seen from $\omega_o = \gamma B_o(1-\sigma)$ after substituting Equ.(1.12) into Equ.(1.8). It is important to note that the separation between peaks increases with increasing B_o because ω_o increases with B_o (Equ.(1.8)). Therefore, a higher B_o provides better spectral resolution.

The separation of resonance frequencies from a selected reference frequency gives chemical shift values, δ, which are calculated as[1,24]

$$\delta = \frac{\upsilon_s - \upsilon_r}{\upsilon_o} \times 10^6, \qquad 1.13$$

where υ_s is the resonance frequency of the nucleus of interest, υ_r is the selected reference frequency (typically TMS, tetramethylsilane in proton MRS) and υ_o is the Larmor frequency. Chemical shifts are expressed as parts per million (ppm), a dimensionless unit, which is independent of the applied fields strength B_o. The conversion between ppm and units of frequency can be obtained using Equ.(1.8). For example, υ_o =127.8 MHz at 3 Tesla. As a result of this, 1 ppm = 127.8 Hz at 3 T. The TMS peak is used as the standard reference signal with a chemical shift of $\delta = 0\ ppm$.

Consider the lactate molecule as an example with a molecular structure of $CH_3CH(OH)COOH$ as illustrated in Figure 1.4(a) and the corresponding ^1H NMR spectrum shown in Figure 1.4(b). The methyl (CH_3) molecular group has 3 protons, which resonate at 1.3 ppm. The CH molecular group has 1 proton, which resonates at 4.1 ppm. Figure 1.4 (b) shows the ^1H NMR spectrum of lactate with two sets of peaks (splitting into several lines, which is discussed in section 1.5). Net peak areas are proportional to the number of protons or nuclei contributing to that resonance, and the relative concentrations of the number of protons are obtained from the peak areas. The total area of the CH_3 peaks should be equal to three times the total area of the CH peaks (assuming no signal losses).

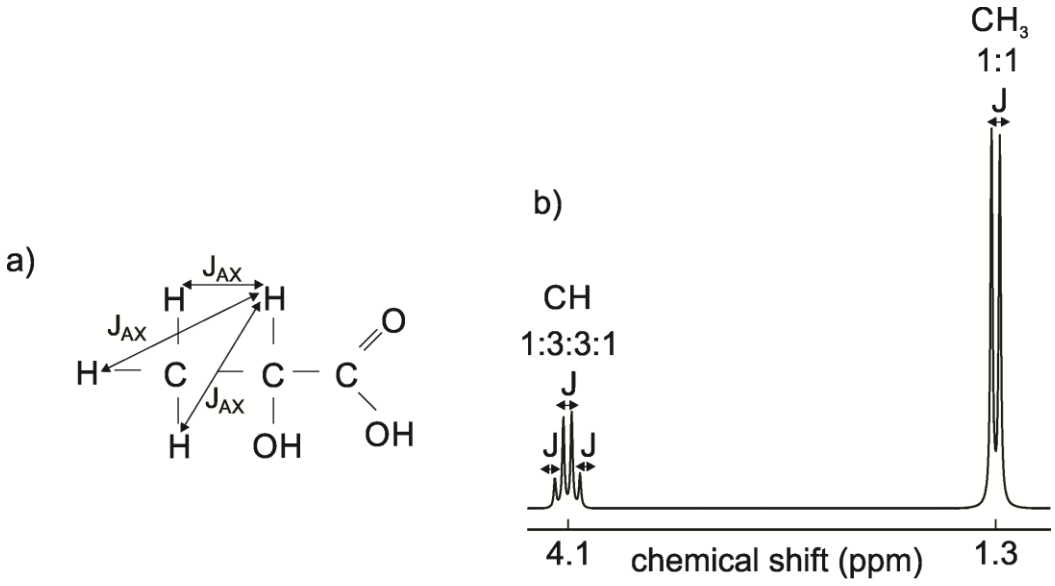

Figure 1.4. The spectrum for lactate. The separation between multiplet peaks belonging to the same molecular group is about J ≈ 6.93 Hz[28]. CH_3 and CH correspond to a doublet peak at 1.3 ppm with relative intensities 1:1, and a quartet peak at 4.1 ppm with relative intensities 1:3:3:1, respectively. CH_3 has 3 protons and causes the coupled CH proton peak to split into a quartet while CH has 1 proton and causes the coupled CH_3 protons to split into a doublet due to the basic principle of spin-spin coupling between two weakly-coupled nuclei.

1.5 J-Coupling

J-coupling is also called scalar coupling, or spin-spin coupling[27]. Water protons do not exhibit J-coupling but many metabolites protons do. If two nuclei on the same molecule are J-coupled, they interact with other through the electron bonds joining them. The interaction due to scalar or spin-spin coupling leads to a splitting of the resonance peaks of the coupled nuclei into multiple smaller peaks[27], as shown in Figure 1.4(b) and Figure 1.5. J is the scalar coupling constant measured in Hz and is independent of the applied magnetic field B_o. Typical J-coupling constants values are in the range of 1-15 Hz for proton-proton coupling (homonuclear ^{1}H coupling)[24].

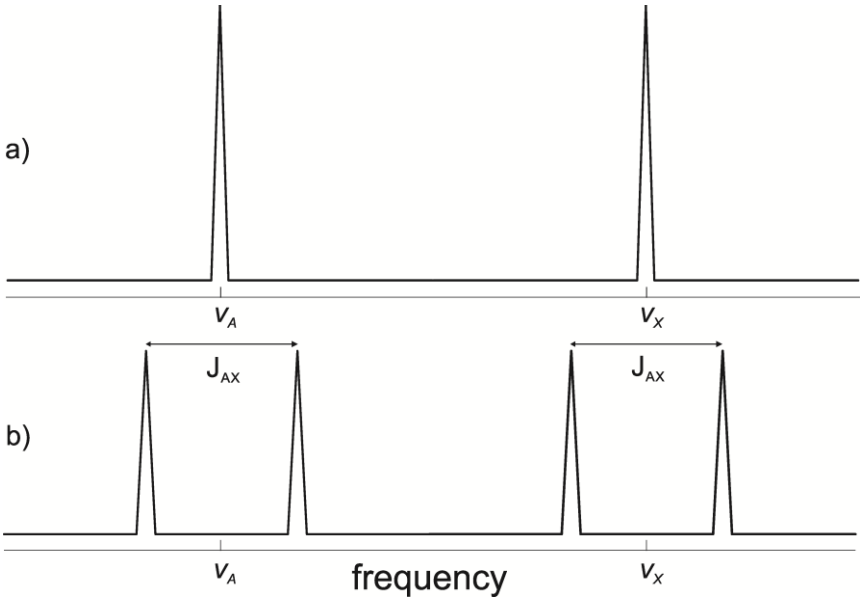

Figure 1.5. Spin-spin coupling interaction between A and X nuclei causes splitting of the single resonance peaks (a) into two resonance lines (b) for A and X. v_A and v_X are the resonance frequencies of the A and X nuclei, respectively. J_{AX} is the J-coupling constant. A and X are labelled as such by letters far away in the alphabet according to a chemistry notation for weakly-coupled spins ($|v_A - v_X| >> J_{AX}$).

Next, let us look at the condition, $|\nu_1 - \nu_2| >> J_{12}$, where ν_1 and ν_2 are the resonance frequencies for nuclei 1 and 2, respectively, and J_{12} is the coupling constant between them. If $\frac{J_{12}}{|\nu_1 - \nu_2|} << 1$, then we have two weakly-coupled nuclei that can be denoted as an AX spin system (according to chemistry notation where nuclei are represented by letters far away in the alphabet if they are weakly-coupled). In general, if a spin 1/2 nuclei is weakly-coupled to n spin 1/2 equivalent nuclei, the resonance splits into n+1 lines (relative heights given by the binominal distribution). Let us revisit the lactate spectrum of Figure 1.4(b). At 3 T, the lactate protons have a chemical shift of $\delta \approx (4.1 - 1.3)\, ppm. 128 \frac{Hz}{ppm} = 360\, Hz$. Since the coupling constant between the nuclei is about $J \approx 6.93\, Hz$ [28], $\frac{J}{\delta}$ is about 0.02, which is much less than 1, implying that lactate can be represented as a weakly-coupled AX_3 spin system at 3 T. The splitting pattern in Figure 1.4(b) follows the rules for weakly-coupled spins.

On the other hand, if $\frac{J_{12}}{|\nu_1 - \nu_2|}$ does not satisfy the condition of being much less than 1, it is called a strongly-coupled spin system that produces second-order spectra. The two nuclei are donated by letters close to each other in the alphabet (e.g. AB). The splitting pattern for strongly-coupled spins is more difficult to predict. Figure 1.6 displays simulated ^{1}H NMR spectra for an AB spin system. The frequency difference (or chemical shift difference $\delta_A - \delta_B$) shown in Figure 1.6 between the A and B resonances increases significantly from the top (where $|\nu_A - \nu_B| = 0$**)** to bottom (where $|\nu_A - \nu_B| >> J_{AB}$) (i.e. compared with the J-coupling constant[29] (by increasing B_o)). Therefore, as B_o increases, the coupling becomes weaker (i.e. $\frac{J_{AB}}{|\delta_A - \delta_B|}$ decreases). This

indicates that the bottom spectrum represents an AX spin system, and gives a first-order spectrum (weakly-coupling) with predictable splitting patterns while the higher spectra represent second-order spectra (strong-coupling).

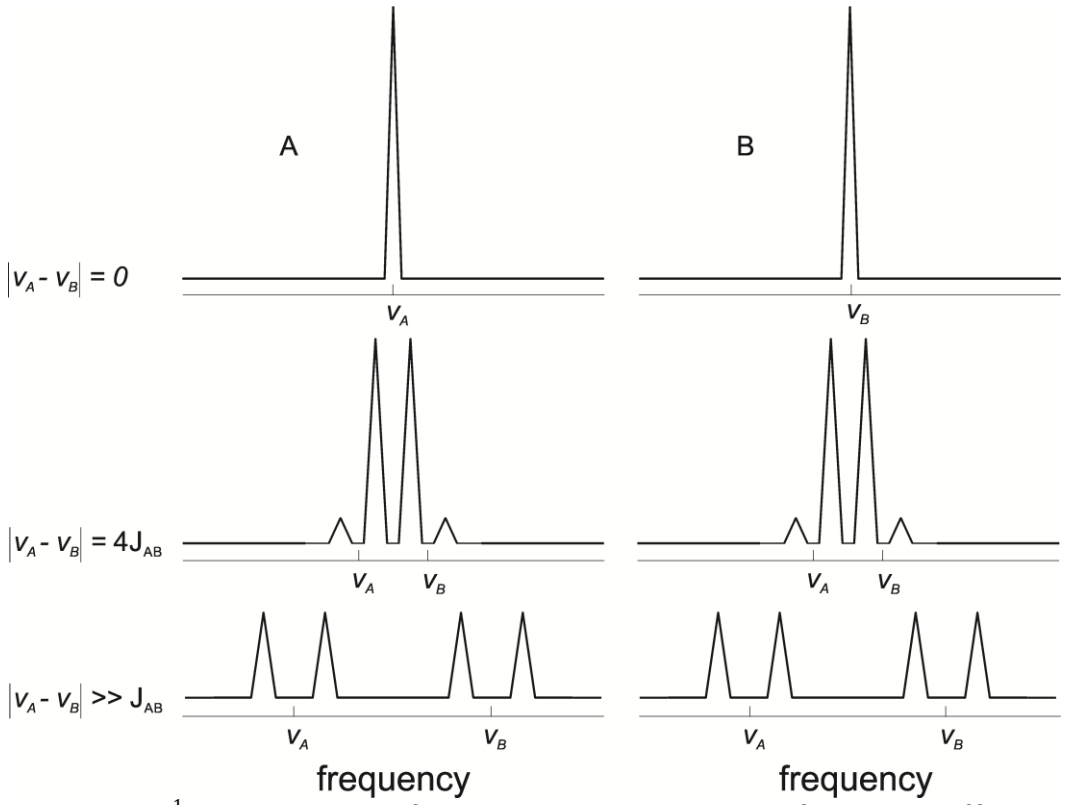

Figure 1.6. ^{1}H NMR spectra for an AB spin system. The frequency difference between the A and B resonances increases clearly from the top (where $|\nu_A - \nu_B| = 0$) -to-bottom (where $|\nu_A - \nu_B| >> J_{AB}$) compared with the J-coupling constant. This indicates that the bottom spectrum represents an AX spin systems with a first-order spectrum (weakly-coupling) with predictable splitting patterns while the higher spectra (e.g. $|\nu_A - \nu_B| = 0$, *and* $|\nu_A - \nu_B| = 4J_{AB}$ represent second-order spectra (strong-coupling) (Adapted from reference[29]). The second order spectra due to strong-coupling do not follow the binomial distribution intensity rule.

1.6 Relaxation

At thermal equilibrium, the net magnetization, M_o, is along B_o as shown Figure 1.1(b) (i.e. $M_z = M_o \equiv$ longitudinal magnetization). There exists no transverse magnetization component (i.e. $M_{xy} = 0$). Once a 90^o RF pulse (i.e. $B_1(t)$) is applied to that spin system, it flips M_o from the z

axis onto a transverse axis such that $M_{xy} = M_o$, and $M_z = 0$. If a 180^o inversion is applied, then M_o is flipped from +z axis to the -z axis, and thus $M_z = - M_o$. After an evolution time t during which relaxation occurs, the spins return to their thermal equilibrium state, where $M_z = M_o$, and $M_{xy} = 0$. This process is known as a recovery of the longitudinal magnetization[31] (because M_z recovers to $+M_o$), and the decay of the transverse magnetization[31] completes (i.e. M_{xy} goes back to zero).

1.6.1 Longitudinal (T_1) or Spin-Lattice Relaxation

The recovery of the longitudinal magnetization, M_z, is called longitudinal or T_1 relaxation. Using the Bloch equation, the longitudinal relaxation is given by a first order rate equation[24,30,31]

$$\frac{dM_z(t)}{dt} = -\frac{M_o - M_z(t)}{T_1}, \qquad 1.14$$

where T_1 is the longitudinal (or spin-lattice) relaxation time. Solving the equation yields[30,31]

$$M_z(t) = M_o(1 - e^{-t/T_1}), \quad \textit{for a } 90^o \textit{ } B_1 \textit{ RF pulse}$$
$$M_z(t) = M_o(1 - 2e^{-t/T_1}), \quad \textit{for a } 180^o \textit{ inversion } B_1 \textit{ RF pulse} \qquad 1.15$$

Longitudinal relaxation curves after applying either a 90^o pulse, or a 180^o pulse are shown in Figure 1.7.

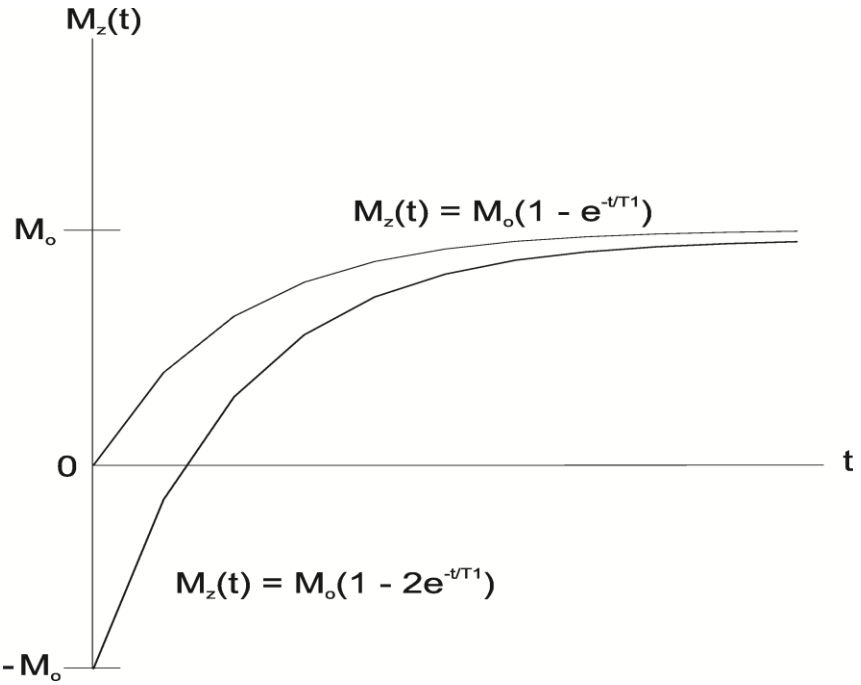

Figure 1.7. Longitudinal relaxation curves after applying either a 90^o pulse (upper curve), or a 180^o pulse (lower curve).

1.6.2 Transverse (T_2) or Spin-Spin Relaxation

The decay of the transverse magnetization M_{xy} is called transverse relaxation, which is also given by a first order differential equation using the Bloch equation[24,30,31]

$$\frac{dM_{xy}}{dt} = -\frac{M_{xy}(t)}{T_2}, \qquad 1.16$$

where T_2 is the transverse (or spin-spin) relaxation time, which is due to spin-spin interaction between the nuclei. Equ.(1.16) can be easily solved to obtain Equ.(1.17), as[30,31]

$$M_{xy}(t) = M_{xy}(0)e^{-t/T_2}, \qquad 1.17$$

where $M_{xy}(0)$ is the transverse magnetization at t = 0 after an RF pulse. Figure 1.8 shows the decay of the transverse magnetization, M_{xy}.

Both T_1, and T_2 values vary with tissue composition, specifically, with the surrounding enviroment[31]. However, T_2 is shorter than T_1 for the nuclear spins[31] and can never exceed T_1.

Therefore, $M_{xy}(t)$ completes its decay before the recovery of $M_z(t)$ totally reaches equilibrium (i.e. $M_z(t) = M_o$).

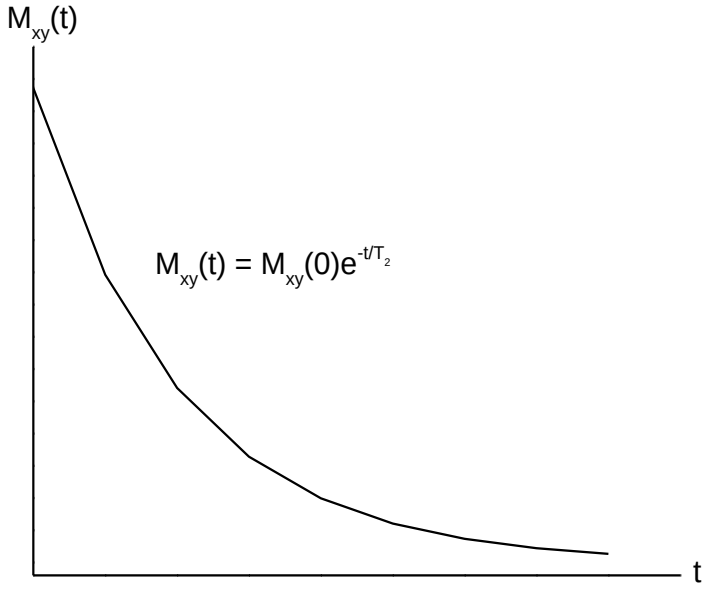

Figure 1.8. The transverse relaxation curve. M_{xy} exponentially decays to zero.

In addition to T_2, another factor is $\mathbf{T_2'}$ that is due to the effect of time independent field variation such as static magnetic field inhomogeneities and magnetic susceptibility differences[24,30]. Thus, if T_2' is taken into account, a new rate constant, T_2^*, is given by[24]

$$\frac{1}{T_2^*} = \frac{1}{T_2} + \frac{1}{T_2'}. \qquad 1.18$$

Since $T_2^* << T_2$, the decay of signal is much faster with T_2^* compared to T_2.

1.7 Spin Echoes

At least two RF pulses are needed to form a spin echo. Figure 1. 9 displays a standard spin-echo experiment obtained from two RF pulses, including time delays (i.e. 90^o - τ - 180^o - τ). The first RF pulse, 90°_x excitation pulse, rotates the spins to the y axis. Then, the spins dephase

during the first time delay τ due to field variations. Next, the second RF pulse, 180°_{x} refocusing pulse, flips the dephasing spins by 180^{o} to recover their direction. After a time τ, the dephasing spins rephase (or refocus). Thus, a spin-echo (SE) is created.

A spin echo can only rephase effects due to $T_2^{'}$ dephasing but not due to T_2 relaxation.

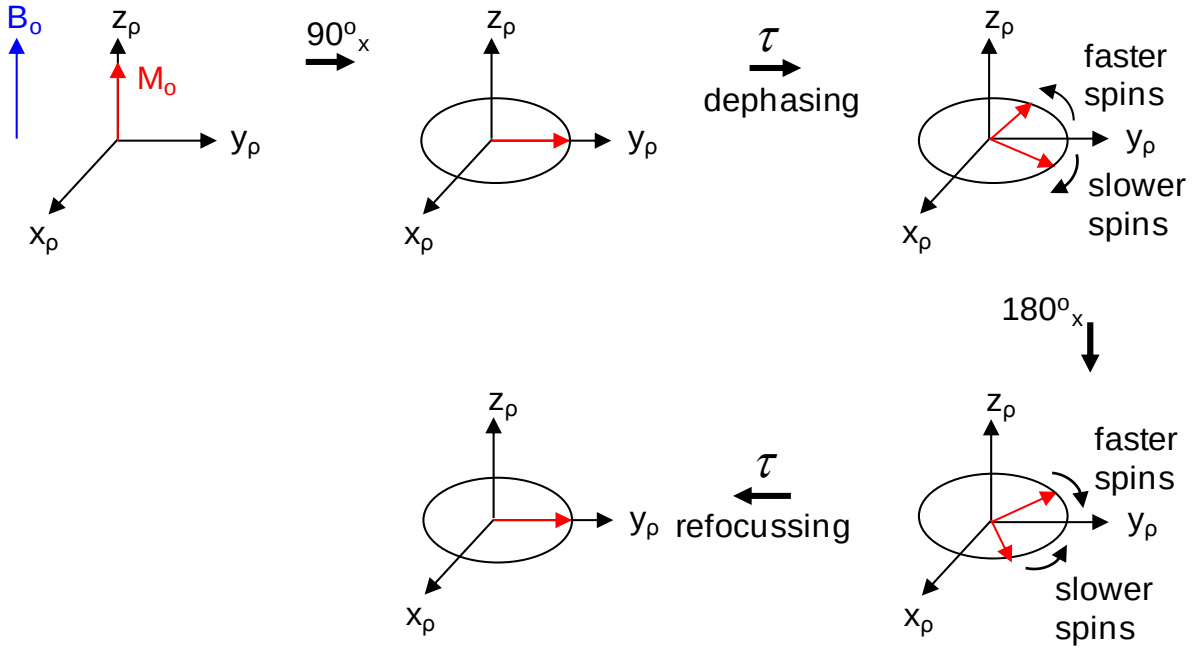

Figure 1. 9. Process of a spin-echo in the rotating frame.

1.8 Stimulated Echoes

At least three RF pulses are required to generate a stimulated echo. Figure 1.10 shows how a stimulated echo is created from three 90^{o} RF pulses as in the STEAM sequences (discussed in section 1.10.2). The net spin magnetization, M_o, and B_o are in the z direction. All the three 90°_{x} RF pulses are along the x direction as shown in Figure 1.15. The first 90°_{x} pulse rotates the M_o in onto the y axis. Complete dephasing occurs during the first TE/2 period due to a dephasing gradient. The second 90°_{x} pulse rotates the c and d magnetization vectors from the y

axis to the z axis. The a and b magnetizations on the x-axis are not affected by the second 90°_{x} pulse. During the mixing time (TM), spoiler gradients eliminate the transverse magnetization but do not affect the longitudinal magnetization. Next, the third 90°_{x} pulse rotates the c and d magnetization vectors in the clockwise direction on to the y axis. During the latter TE/2 period the transverse magnetization components c and d are rephased by the gradient applied during that time period.

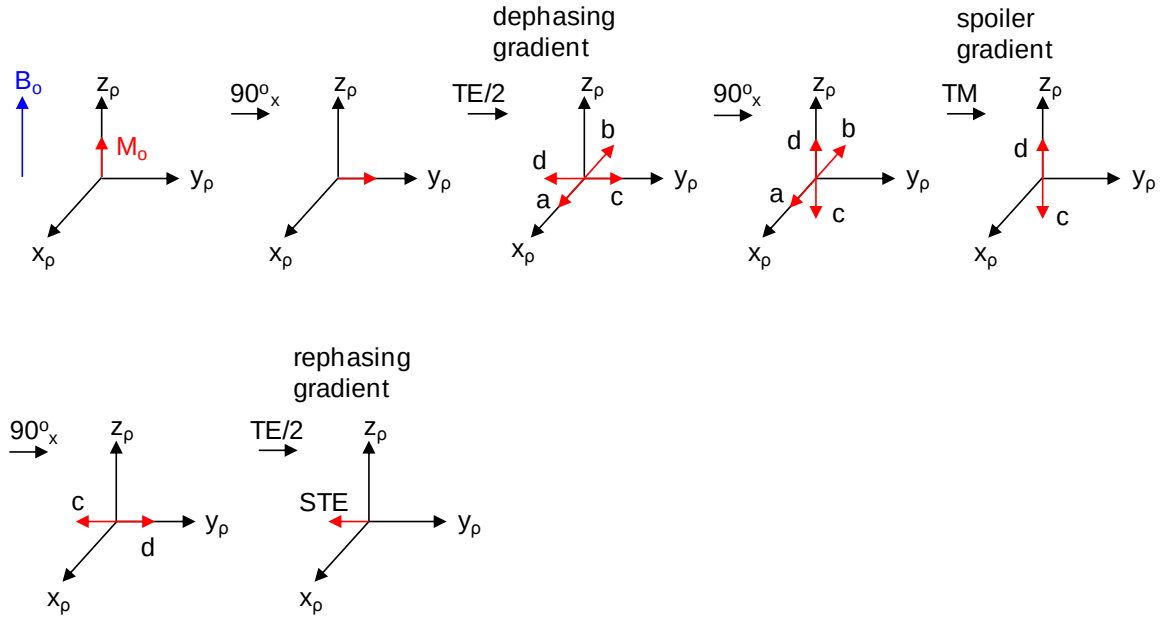

Figure 1.10. Generation of a stimulated echo from three 90° RF pulses (adapted from reference[36]).

1.9 Spatial Localization in In-Vivo NMR (Slice Selection)

Linear magnetic field gradients (G_x, G_y, G_z) vary linearly in x, y, and z directions in the static homogeneous B_o field due to gradient coils (i.e. $G_x = dB_z/dx$, $G_y = dB_z/dy$, $G_z = dB_z/dz$, where $B_z = B_o$, and B_o is in the z direction)[30,31,32]. The Larmor equation (i.e. the resonance equation, $\omega_o = \gamma B_o$ from Equ.(1.8)) is obtained in the absence of gradients. In the presence of a

magnetic field gradient G_z along the z direction, the total effective magnetic field is given by[24,30,31,32]

$$B(z) = B_o + zG_z, \tag{1.19}$$

where z is the distance from the magnet iso-center (where $G_z = 0$). The modified resonance equation (Equ.(1.8)) is[24,30,31,32]

$$\omega(z) = \gamma B(z) = \gamma B_o + \gamma z G_z. \tag{1.20}$$

This means that the resonance frequency, $\omega(z)$, now depends on position, *z*, and the gradient also effects the resonance frequency. The frequency difference[30,31,32] can also be calculated from Equ.(1.20),

$$\Delta\omega = \omega_{z_1} - \omega_{z_2} = \gamma G_z \Delta z, \tag{1.21}$$

where Δz is the distance between two positions z_1 and z_2. The resonance frequency difference (i.e. the bandwidth of resonance frequency), $\Delta\omega$, has to be equal to the frequency bandwidth of the RF pulse (BW_{rf}) to excite spins in the selected slice under the slice selection condition, i.e. $\Delta\omega = BW_{rf}$. Therefore, Equ.(1.21) can be rewritten as[30,31,32]

$$BW_{rf} = \gamma G_z \Delta z, \tag{1.22}$$

where γ is the gyromagnetic ratio, G_z is the slice select gradient amplitude along the z direction, and Δz is the slice thickness. The BW_{rf} expresses the excited slice width. The unit of the gradients is either Gauss/centimeter (G/cm) or milliTesla/meter (mT/m), where 1 G/cm = 10 mT/m, and the BW_{rf} is expressed in unit of Hz. The equation also applies to gradients applied in other directions.

Signal can be obtained from only the selected slice by the use of a slice selective RF pulse applied in conjunction a linear magnetic field gradient, as shown in Figure 1.11. The

frequency of the RF pulse is needed to define the central position of the excited slice, as shown in Equ.(1.20). The excited slice is perpendicular to z axis (i.e. G_z) shown in Figure 1.11.

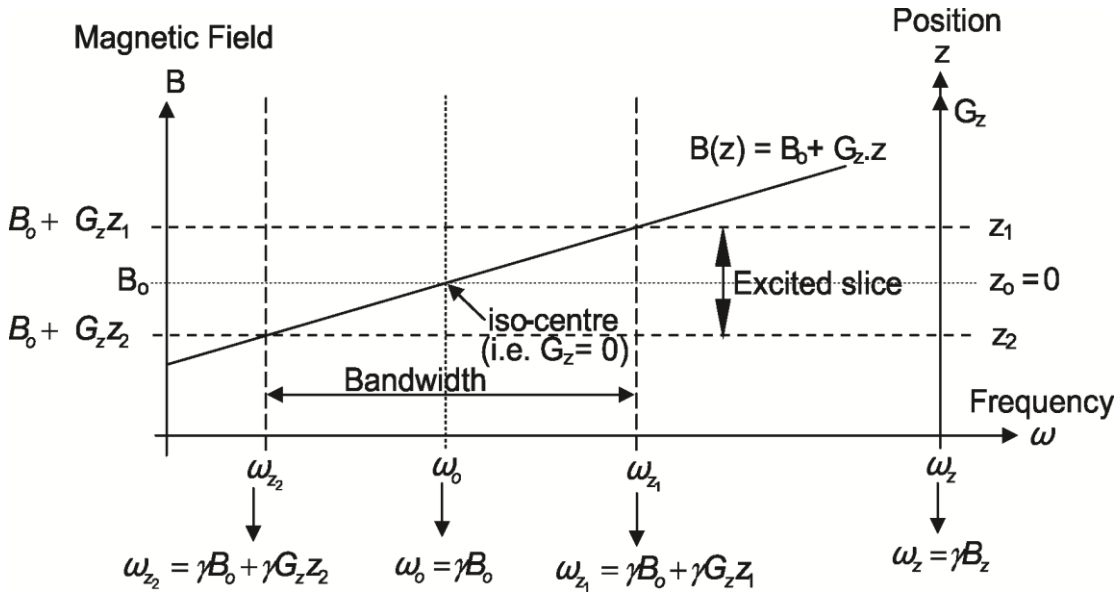

Figure 1.11 shows the slice selection after a slice selective RF pulse and a linear magnetic field gradient (G_z) in the z direction are applied. The slice is selected (two dash lines) perpendicularly to the slice selection gradient (G). B_o is the static magnetic field, and B is total effective magnetic field. ω_o is the resonance frequency at the iso-centre (i.e.where G = 0), and ω_z is the resonance frequency at position z. The excited slice is perpendicular to z axis. $B = B_o$ in the absence of field gradients, and $B_z = B_o + G_z.z$ in the presence of the field gradient.

Figure 1.12 shows a sinc slice selective pulse applied simultaneously with a slice selective gradient. A dispersion in phase of the transverse magnetization occurs by the process[31]. This is reversed by the application of a negative gradient that has half the area of the slice selection lobe.

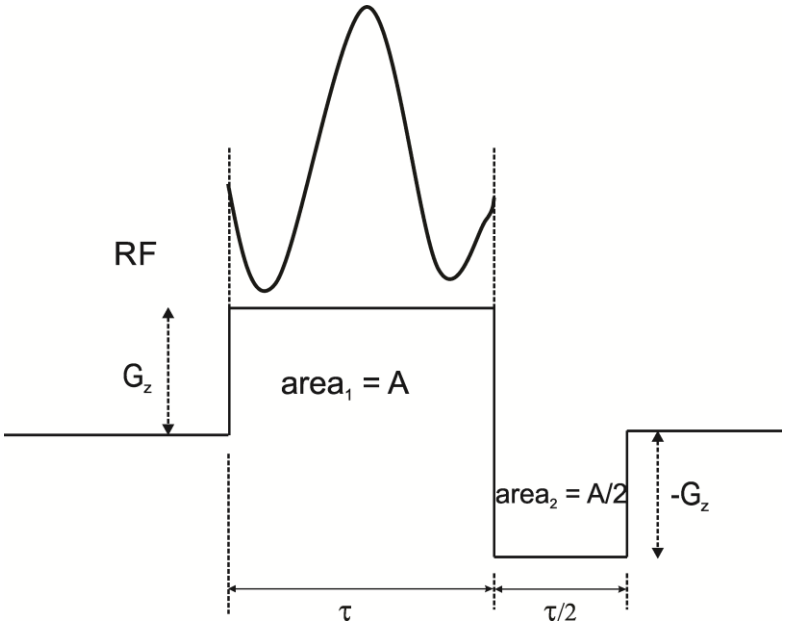

Figure 1.12. The slice selection and rephasing gradient component of slice selection processes. The slice selection gradient lobe has twice the area of the rephasing gradient lobe (i.e. area of $G_z\tau$).

1.10 Methods in In-Vivo Magnetic Resonance Spectroscopy

There are two common single-shot pulse sequences used in in-vivo proton MRS for single-voxel localization using B_o magnetic field gradients. One is Point RESolved Spectroscopy[33,34] (PRESS), and the other is Stimulated Echo Acquisition Mode[35,36] (STEAM). Both are 3D spatial localization techniques that employ three radio frequency (RF) pulses applied with slice selection in three orthogonal directions. The signal is acquired from a given spatially localized cube (single-voxel), as shown in Figure 1.13.

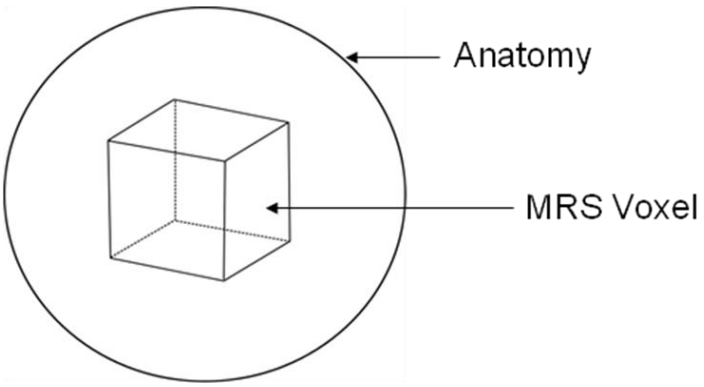

Figure 1.13. Standard in-vivo MRS sequences such as PRESS or STEAM yield signal from a defined 3D cubic volume (single-voxel).

1.10.1 PRESS (Point RESolved Spectroscopy)

Figure 1.14 shows a PRESS sequence which consists of three slice selective RF pulses, namely, one slice selective 90^o RF excitation pulse followed by two slice selective 180^o refocusing pulses. The 90^o pulse yields transverse magnetization from a slice of interest. PRESS is a double spin-echo method that is characterized by two echo times, TE_1 and TE_2 (Figure 1.14). The total echo time is $TE = TE_1 + TE_2$. Signal of the first echo comes from a column that is at the intersection of the signal selected by the slice selective 90^o pulse and the first 180^o pulse. The acquired signal is the outcome of the second spin-echo which originates from a cube where the three slices intersect. G_x, G_y, and G_z are magnetic field slice selection gradients applied in x, y, and z directions, respectively. Spoiler gradients dephase signal coming from outside the volume of interest, and eliminate any unwanted signal coming from spins that experience imperfect 180^o pulses.

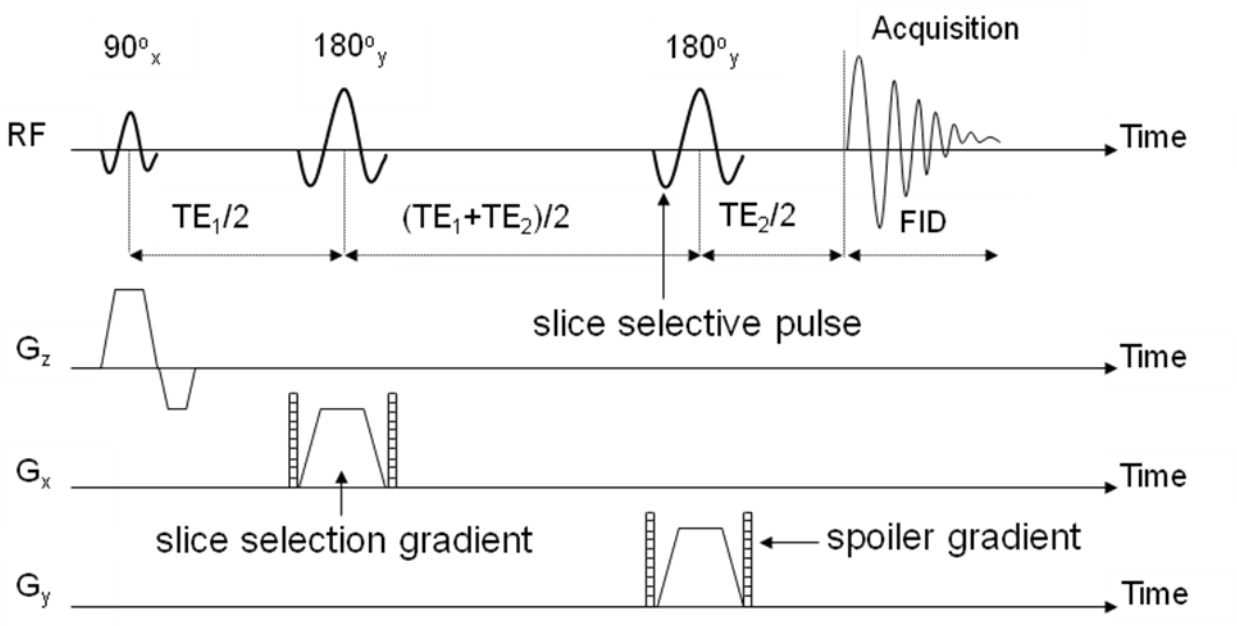

Figure 1.14. PRESS pulse sequence for single-voxel localization (i.e. 3D spatial localization). G_x, G_y, and G_z are slice selection gradients in x, y, and z directions, respectively. Spoiler gradients eliminate any unwanted signal coming from spins that experience imperfect 180° pulses. FID (free induction decay) is the acquired signal.

Amplitude of the generated signal in PRESS sequence is given by[37]

$$S = S_0\left[1-2\exp\left(-\frac{\left(TR-\frac{TE}{2}\right)}{T_1}\right)+\exp\left(-\frac{TR}{T_1}\right)\right].\exp\left(-\frac{TE}{T_2}\right). \qquad 1.23$$

For the case of no J-coupling and TR >> TE, the signal from Equ.(1.23) becomes

$$S = S_0\left(1-e^{-\frac{TR}{T_1}}\right)e^{-\frac{TE}{T_2}}, \qquad 1.24$$

where S is the signal at time equal to TE, S_0 is the initial signal at TE = 0, TR is repetition time, TE is total echo time, T_1 the is longitudinal relaxation time, and T_2 is the transverse relaxation time.

1.10.2 STEAM (STimulated Echo Acquisition Mode)

Figure 1.15 shows a standard STEAM sequence which consists of three slice selective of 90^o RF pulses. STEAM yields a stimulated echo from the region where all three orthogonal planes intersect. Spoiler gradients are employed to dephase and eliminate spin echoes, and undesired signal so that a 'clean' stimulated echo can be obtained. They also dephase and rephase the desired signal. The mixing time (TM) is placed between the second and third 90^0 pulses in the STEAM sequence. Spoilers during TM eliminate transverse magnetization, preventing spin echo formation. The STEAM sequence generates a desired stimulated echo explained in section 1.8.

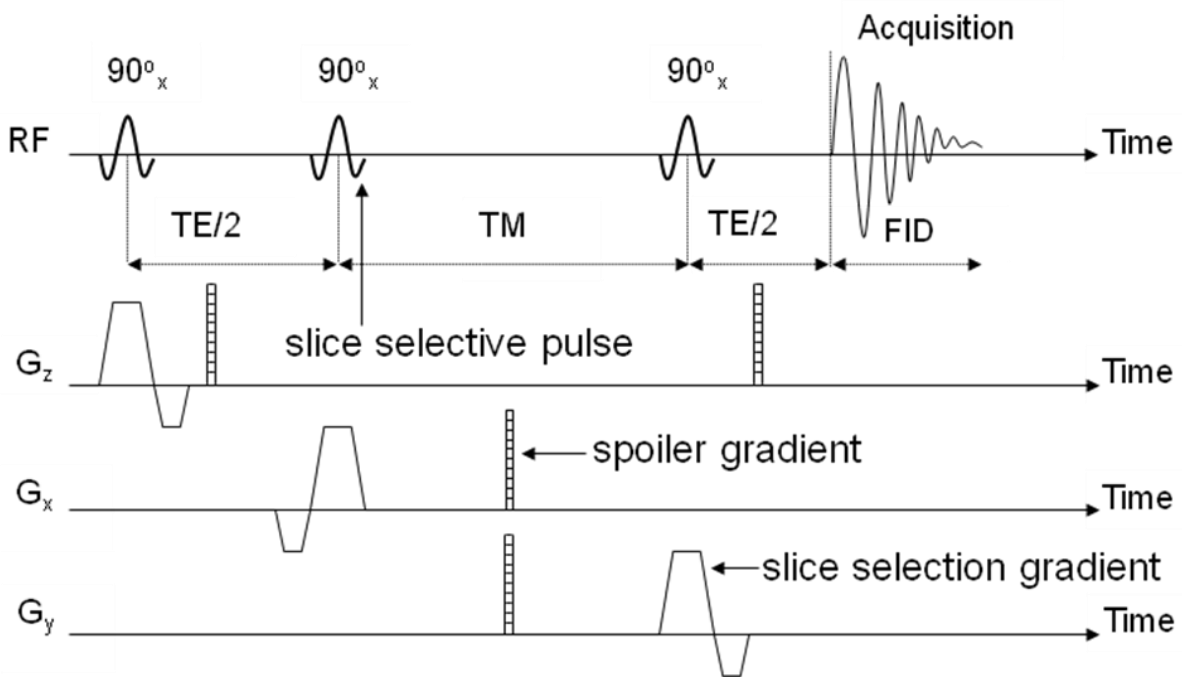

Figure 1.15. STEAM pulse sequence for single-voxel localization (i.e. 3D spatial localization). Three 90^o RF pulses are seen. Spoiler gradients dephase spin echoes and any undesired signal so that a 'clean' stimulated echo can be obtained. Spoiler during TM gets rid of transverse magnetization. The spoiler in the first TE/2 dephases the net spin magnetization (M_o) but rephases it in the last TE/2. Refocusing lobes of the 2^{nd} and 3^{rd} 90^o pulses cannot be applied during TM because the desired signal is longitudinal during that period.

Amplitude of the generated signal by the STEAM sequence is given by[38]

$$S = \frac{S_0}{2}\left[1-\exp\left(-\frac{TR-TM-\frac{TE}{2}}{T_1}\right)\right].\exp\left(-\frac{TM}{T_1}\right).\exp\left(-\frac{TE}{T_2}\right). \qquad 1.25$$

For the case of no J-coupling and TR >> TE + TM, the signal from Equ.(1.25) becomes as

$$S = \frac{S_0}{2}\exp\left[-\left(\frac{TM}{T_1}+\frac{TE}{T_2}\right)\right]\left[1-e^{-\frac{TR}{T_1}}\right]. \qquad 1.26$$

It is important to note that STEAM yields half the signal ($\frac{S_0}{2}$) of PRESS at TE = 0 due to the nature of the stimulated echo.

1.11 J – Coupling Evolution During PRESS and STEAM

PRESS and STEAM sequences generate spin-echo and stimulated-echo signals, respectively. We consider here for simplicity a weakly-coupled AX spin system. Ignoring relaxation, during a spin-echo experiment (e.g. PRESS), the evolution of in-phase A_x coherence (which exists after the 90°_y excitation pulse is applied) is given by[29]

$$A_x \rightarrow \left[A_x \cos(\pi J T_E) + 2A_y X_z \sin(\pi J T_E)\right], \qquad 1.27$$

where A_x and $2A_yX_z$ are termed in-phase and anti-phase coherences, respectively, T_E is the echo time, and J is the coupling constant between the A and X spins. Figure 1.16(a) shows simulated signal from a spin-echo experiment (e.g. PRESS) for the evolution of in-phase A_x magnetization for the A spin of an AX spin system.

On the other hand, the net observable signal for spin A after the application of the STEAM sequence is given by[29]

$$S(T_E + T_M) = \frac{1}{2}\left(\cos^2\left(\frac{\pi J T_E}{2} \right) - \frac{1}{2}\sin^2\left(\frac{\pi J T_E}{2} \right)\left[1 - \cos\left(\frac{\Delta\omega_{AX} T_E}{2} \right) \right] \cos\left(\Delta\omega_{AX} T_M \right) \right), \qquad 1.28$$

where $\Delta\omega_{AX} = |\omega_A - \omega_X|$ is the chemical shift difference between spin A and spin X in Hz, and T_M is the mixing time. The $\cos^2\left(\frac{\pi J T_E}{2} \right)$ comes from single-quantum coherences of spin A which were longitudinal during TM. The second term comes from zero-quantum coherences during TM that resulted from contribution from both the A and the X spins. Quantum coherences are beyond the scope of this thesis but it is clear that the response of coupled spins to STEAM is for more complex than the response to PRESS. The dependence of signal on the chemical shift difference causes rapid oscillations in the signal, as shown in Figure 1.16(b). The evolution of strongly coupled spins during PRESS and STEAM are more complicated than that of a simple AX spin system.

The effects of J-coupling evolution during PRESS and STEAM affect the observed lineshape, and intensity of peaks[39,40,41,42,43]. Signal losses that occur due to J-coupling decrease measured apparent T_2 values because of the superposition of decay due to J-coupling and T_2 relaxation[14,44,45,46,47].

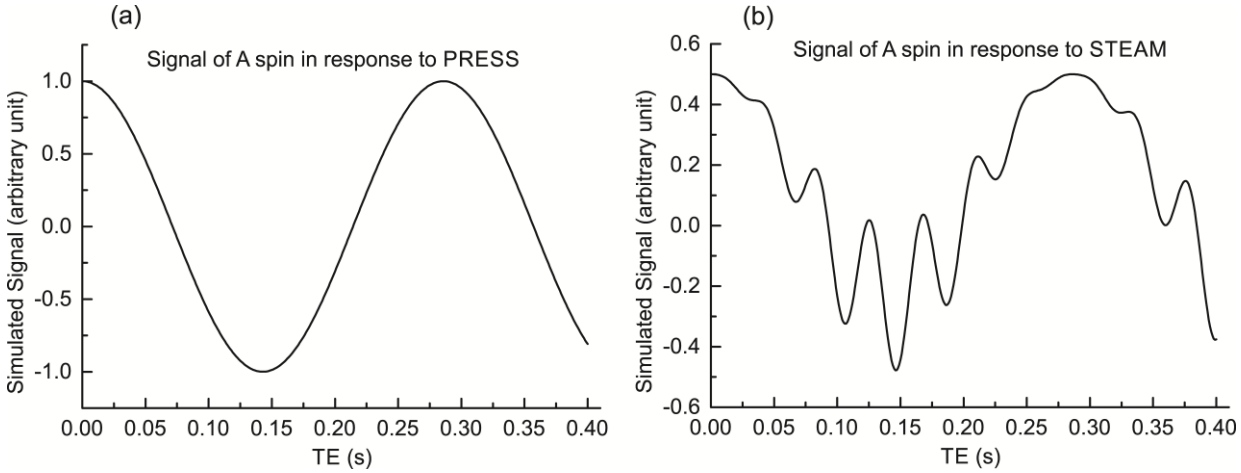

Figure 1.16. Simulated signal evolution for observable signal from the A spin of an AX spin system (a) from PRESS with J = 7 Hz, (b) from STEAM with J = 7 Hz, $\Delta\omega_{AX} = 300\,Hz$, and TM = 20 ms as a function of TE. The dependence on chemical shift difference (due to chemical shift evolution during TM) causes rapid oscillations in signal response to the STEAM sequence.

1.12 Some Single-Voxel MRS Parameters

Some relevant parameters in *in-vivo* PRESS and STEAM are: the repetition time (TR) which is the time from application of initial excitation pulse to its next application (~ 1 - 3 seconds), the echo time (TE) which is usually 30 - 40 ms in short-TE MRS, the number of averages (N_{AV}) which is increased to increase signal to noise ratio (SNR) as $SNR\alpha\sqrt{N_{AV}}$, and $N_{AV} \approx 32$ - 256, and a voxel size is typically within 2x2x2 cm^3.

1.13 References

1. D. G. Gadian. Nuclear magnetic resonance and its applications to lining systems. Oxford University Press, New York, US (1982).

2. E. Lunati, P. Farace, E. Nicolato, C. Righetti, P. Marzola, A. Sbarbati, F. Osculati. Polyunsaturated fatty acids mapping by ^{1}H NMR-chemical shift imaging. Magnetic Resonance in Medicnice **46,** 879–883 (2001).

3. J. Machann, N. Stefan, F. Schick. ^{1}H MR spectroscopy of skeletal muscle, liver and bone marrow. Eur J Radiol **67**, 275–284 (2008).

4. C. Boesch, J. Machann, P. Vermathen, F. Schick. Role of proton MR for the study of muscle lipid metabolism. NMR Biomed **19**, 968–988 (2006).

5. S. S. Velan, N. Said, C. Durst, S. Frisbee, J. Frisbee, R. R. Raylman, M. A. Thomas, V. M. Rajendran, R. G. Spencer, S. E. Alway. Distinct patterns of fat metabolism in skeletal muscle of normal-weight, overweight, and obese humans. Am J Physiol Regul Integr Comp Physiol **295**, R1060–R1065 (2008).

6. R. Borra, R. Lautamäki, R. Parkkola, M. Komu, P. E. Sijens, K. Hällsten, J. Bergman, P. Iozzo, P. Nuutil. Inverse association between liver fat content and hepatic glucose uptake in patients with type 2 diabetes mellitus. Metabolism Clinical and Experimental **57**, 1445–1451 (2008).

7. A. Kotronen, L. Juurinen, M. Tikkainen, S. Vehkavaara, H. Yki-Jarvinen. Increased liver fat, impaired insulin clearance, and hepatic and adipose tissue insulin resistance in type 2 diabetes. Gastroenterology **135**, 122–130 (2008).

8. F. Fischbach, H. Bruhn. Assessment of in vivo ^{1}H magnetic resonance spectroscopy in the liver: a review. Liver Int **28**, 297–307 (2008).

9. T. Yokoo, M. Bydder, G. Hamilton, M. S. Middleton, A. C. Gamst, T. Wolfson, T. Hassanein, H. M. Patton, J. E. Lavine, J. B. Schwimmer, C. B. Sirlin. Nonalcoholic fatty liver disease: diagnostic and fat grading accuracy of low-flip-angle multiecho gradient-recalled-echo-MR imaging at 1.5 T. Radiology **251**, 67–76 (2009).

10. K. E. Jensen, M. Jensen, P. Grundtvig, C. Thomsen, H. Karle, O. Henriksen. Localized in vivo proton spectroscopy of the bone marrow in patients with leukemia. Magnetic Resonance Imaging **8**, 779–789 (1990).

11. M. Kumar, N. R. Jagannathan, V. Seenu, S. N. Dwivedi, P. K. Julka, G. K. Rath. Monitoring the therapeutic response of locally advanced breast cancer patients: sequential in vivo proton MR spectroscopy study. Journal of Magnetic Resonance Imaging **24**, 325–332 (2006).

12. A. Oriol, D. Valverde, J. Capellades, M. E. Cabanas, J-M. Ribera, C. Arus. In vivo quantification of response to treatment in patients with multiple myeloma by ^{1}H magnetic resonance spectroscopy of bone marrow. Magn Reson Mater Phys **20**, 93–101 (2007).

13. J. Lundbom, A. Hakkarainen, S. Soderlund, J. Westerbacka, N. Lundbom, M-R. Taskinen. Long-TE ^{1}H MRS suggests that liver fat is more saturated than subcutaneous and visceral fat. NMR in Biomedicine **24**, 238-245 (2011).

14. G. Hamilton, M. S. Middleton, M. Bydder, T. Yokoo, J. B. Schwimmer, Y. Kono, H. M.Patton, J. E. Lavine, and C. B. Sirlin. Effect of PRESS and STEAM sequences on magnetic resonance spectroscopic liver fat quantification. Journal of Magnetic Resonance Imaging **30**, 145-152 (2009).

15. J. Lundbom, A. Hakkarainen, B. Fielding, S. Soderlund, J. Westerbacka, M-R. Taskinen, N. Lundbom. Characterizing human adipose tissue lipids by long echo time ^{1}H-MRS in vivo at 1.5 Tesla: validation by gas chromatography. NMR in Biomedicine **23**, 466-472 (2010).

16. E. Mosconi, M. Fontanella, D. M. Sima, S. V. Huffel, S. Fiorini, A. Sbarbati, P. Marzola. Investigation of adipose tissues in Zucker rats using in vivo and ex vivo magnetic resonance spectroscopy. Journal of Lipid Research **52**, 330–336 (2011).

17. K. Strobel, J. van den Hoff, J. Pietzsch. Localized proton magnetic resonance spectroscopy of lipids in adipose tissue at high spatial resolution in mice in vivo. Journal of Lipid Research **49,** 473 – 480 (2008).

18. Q. He, P. Shkarin, R. J. Hooley, D. R. Lannin, J. C. Weinreb, V. I. J. Bossuyt. In vivo MR spectroscopic imaging of polyunsaturated fatty acids (PUFA) in healthy and cancerous breast tissues by selective multiple quantum coherence transfer (Sel-MQC): A preliminary study. Magnetic Resonance in Medicine **58**, 1079-1085 (2007).

19. H. Zhu, D. Rubin, Q. He. The fast spiral-SelMQC technique for in vivo MR spectroscopic imaging of polyunsaturated fatty acids in human breast tissue. Magnetic Resonance in Medicine **67**, 8-19 (2012).

20. M. A. Korteweg, W. B. Veldhuis, W. P.Th. M. Mali, S. C. E. Diepstraten, P. R. Luijten, M. A. A. J. van den Bosch, R. M. J. C. Eijkemans, P. J. van Diest, D. W. J. Klomp. Investigation of lipid composition of dissected sentinel lymph nodes of breast cancer patients by 7T Proton MR Spectroscopy. Journal Magnetic Resonance Imaging **35**, 387–392 (2012).

21. J. Ren, I. Dimitrov, A. D. Sherry, C. R. Malloy. Composition of adipose tissue and marrow fat in humans by ^{1}H NMR at 7 Tesla. Journal of Lipid Research **49**, 2055-2062 (2008).

22. A. Troitskaia, B. G. Fallone, A. Yahya. Long echo time proton magnetic resonance spectroscopy for estimating relative measures of lipid unsaturation at 3 T. Journal Magnetic Resonance Imaging **37**, 944-949 (2013).

23. P. W. Atkins and J. de Paula. Atkins' Physical Chemistry. Oxford University Press, Oxford, UK (2006).

24. R. A. De Graaf. In vivo NMR spectroscopy. John Wiley & Sons Ltd, Baffins Lane, Chichester, England (2002).

25. W. G. Proctor and F.C. Yu. The dependence of a nuclear magnetic resonance frequency upon chemical compound. Phys. Rev. **77**, 717-717 (1950).

26. W. C. Dickinson. Dependence of the ^{19}F nuclear resonance position on chemical compound. Phys. Rev. **77**, 736-737 (1950).

27. N. F. Ramsey and E. M. Purcell. Interactions between nuclear spins in molecules. Phys. Rev. **85**, 143-144 (1952).

28. P. B. Kingsley. Scalar coupling and zero-quantum coherence relaxation in STEAM: Implications for spectral editing of lactate. Magnetic Resonance in Medicine **31**, 315-319 (1994).

29. R. A. DE Graaf and D. L. Rothman. In vivo detection and quantification of scalar coupled ^{1}H NMR resonances. Concepts in Magnetic Resonance **13**, 32-76 (2001).

30. P. T. Callaghan. Principles of nuclear magnetic resonance microscopy. Oxford University Press, New York, US (1993).

31. Z. P. Liang, P. C. Lauterbur. Principle of magnetic resonance imaging. The Institute of Electrical and Engineers, Inc., New York, USA (2000).

[32.] Y. Xia. Contrast in NMR imaging and microscopy. Concepts in Magnetic Resonance **8**, 205-225 (1996).

[33.] P. A. Bottomley. Selective volume method for performing localized NMR spectroscopy. U.S. Patent 4,480,228 (1984).

[34.] R. J. Ordidge, M. R. Bendall, R. E. Gordon, and A. Connely. Volume selection for in vivo spectroscopy. Magnetic Resonance in Biology and Medicine, McGraw Hill, 387-397 (1985).

[35.] J. Frahm, K-D. Merboldt, W. Hanicke. Localized proton spectroscopy using stimulated echoes. Journal of Magnetic Resonance **72**, 502-508 (1987).

[36.] D. Burstein. Stimulated echoes: description, applications, practical hints. Concepts in Magnetic Resonance **8**, 269-278 (1996).

[37.] F. Traber, W. Block, R. Lamerichs, J. Gieseke, H. H. Schild. ^{1}H metabolite relaxation times at 3.0 Tesla: measurements of T_1 and T_2 values in normal brain and determination of regional differences in transverse relaxation. Journal of Magnetic Resonance Imaging **19**, 537-545 (2004).

[38.] G. Helms. Analysis of 1.5 Tesla proton MR spectra of human brain using LCmodel and an imported basis set. Magnetic Resonance Imaging **17**, 1211-1218 (1999).

[39.] A. H. Wilman, P. S. Allen. The response of the strongly coupled AB system of citrate to typical ^{1}H MRS localization sequences. Journal of Magnetic Resonance B **107**, 25-33 (1995).

[40.] A. H. Wilman, P. S. Allen. Observing N-acetyl aspartate via both its N-acetyl and its strongly coupled aspartate groups in *in–vivo* proton magnetic resonance spectroscopy. Journal of Magnetic Resonance B **113**, 203-213 (1996).

41. H. Kim, R. B. Thompson, C. C. Hanstock, P. S. Allen.Variability of metabolite yield using STEAM or PRESS sequences *in–vivo* at 3.0 T, illustrated with myo-Inositol. Magnetic Resonance in Medicine **53**, 760-769 (2005).

42. R. B. Thompson, P. S. Allen. Sources of variability in the response of coupled spins to the PRESS sequence and their potential impact on metabolite quantification. Magnetic Resonance in Medicine **41**, 1162–1169 (1999).

43. R. B. Thompson, P. S. Allen. Response of metabolites with coupled spins to the STEAM sequence. Magnetic Resonance in Medicine **45**, 955-965 (2001).

44. P. A. Hardy, R. M. Henkelman, J. E. Bishop, C. S. Poon, D. B. Plewes. Why fat is bright in RARE and fast spin-echo imaging. Journal of Magnetic Resonance Imaging **2**, 533-540 (1992).

45. L.A. Stables, R. P. Kennan, A. W. Anderson, R. T. Constable, J. C. Gore. Analysis of J coupling-induced fat suppression in DIET imaging. Journal of Magnetic Resonance **136**, 143-151 (1999).

46. L.A. Stables, R. P. Kennan, A. W. Anderson, J. C. Gore. Density matrix simulations of the effects of J coupling in spine echo and fast spin echo imaging. Journal of Magnetic Resonance **140**, 305-314 (1999).

47. T. Ernst, J. Hennig. Coupling effects in volume selective ^{1}H spectroscopy of major brain metabolites. Magnetic Resonance in Medicine **21**, 82-96 (1991).

Chapter 2 MRS of Lipids

2.1 Lipids

Lipids are kinds of fats, oils, and waxes, and most of them are insoluble in water but soluble in nonpolar organic solvents. Lipids, like carbohydrates, consist of carbon (C), hydrogen (H), and oxygen (O) atoms. The empirical formula of a carbohydrate is given by $C_mH_nO_p$ (where m, n, p are integers). In this combination, the number of hydrogen atoms is the highest, and the number of oxygen atoms is the lowest. The ratio of hydrogen-to-carbon is generally near 2. For example, the ratio of H/C is 1.89 for the molecule of oleic acid (CH_3 – $(CH_2)_7$ – CH = CH – $(CH_2)_7$ – COOH). Additionally, lipids can also consist of small percentages of phosphorus, nitrogen, or sulfur[1].

Lipids yield energy after being broken down in the body. Unused lipids in the body are stored in fat deposits. For adult men, 12 - 18% of the total body weight is lipids, and for adult women amount of lipids is 18 - 24% of their total body weight[1]. There are many types of lipids in the body[1,2]. Fatty acids are the most common building block from most lipids.

2.2 Fatty Acids

Fatty acids (FA) are a type of lipid which contains long carbon chains that are attached to hydrogen atoms (Figure 2.1 and Figure 2.2). A carboxyl (–COOH) group is attached at one end, and a methyl (CH_3) is attached to the other end of the carbon chain. The carboxyl can also be written in terms of a carbon and a hydroxyl (–OH) group.

Fatty acids may be divided into two groups: saturated fatty acids (SFA), and unsaturated fatty acids (UFA)[3].

2.2.1 Saturated Fatty Acids

Saturated fatty acids have no double bonds between carbon atoms, and primarily consists of myristic, palmitic, and stearic acids[3]. Figure 2.1 shows that each carbon atom, except for the ones at each end, binds to two hydrogen atoms, and two other adjacent carbon atoms. Thus, each carbon atom has four single covalent bonds in a saturated fatty acid (e.g. lauric acid: CH_3 – $(CH_2)_{10}$ – COOH)). The carbon atom at the end binds to three hydrogen atoms (i.e. CH_3).

Saturated

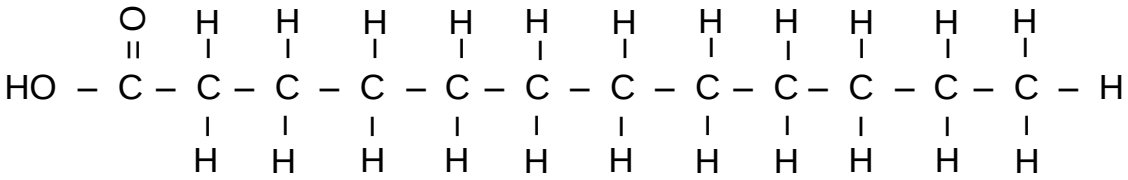

Figure 2.1. Molecular structure of a saturated fatty acid, lauric acid ($C_{12}H_{24}O_2$). A carboxyl (– COOH) group is attached at one end, and a methyl (CH_3) group is attached to the other end of the carbon chain. No double bonds are present between carbon atoms.

2.2.2 Unsaturated Fatty Acids

Unsaturated fatty acids are mainly classified as monounsaturated fatty acids (MUFA), and polyunsaturated fatty acids (PUFA)[3]. A monounsaturated fatty acid has only one double bond between carbon atoms, and a polyunsaturated fatty acid contains more than one double bond between carbon atoms in the carbon chains.

Unsaturated

Oleic

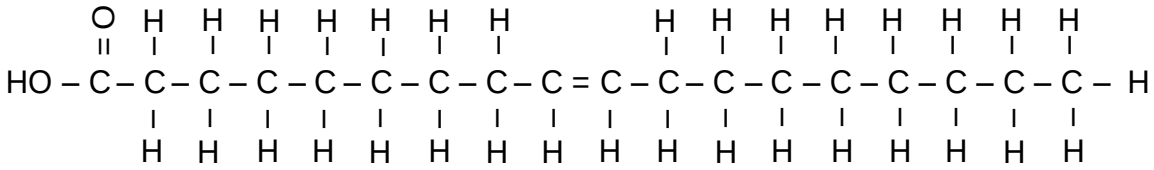

Linoleic

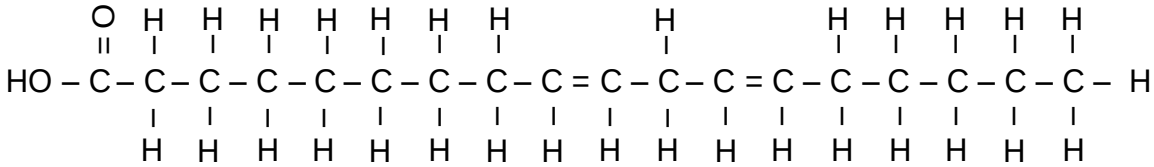

Linolenic

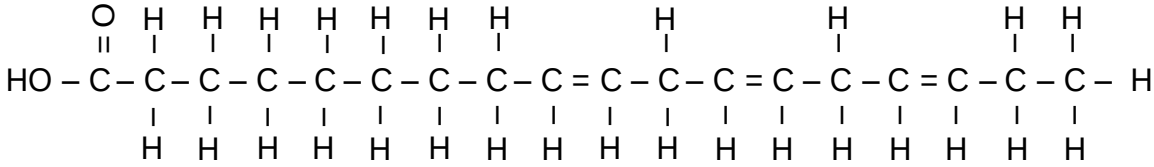

Figure 2.2. Molecular structure of unsaturated fatty acids (oleic, linoleic, and linolenic). Oleic acid ($C_{18}H_{34}O_2$) contains a single double bound that is placed at the 9th carbon from the methyl (CH_3) end. Linoleic acid ($C_{18}H_{32}O_2$) contains two double bonds where the first double bonds is placed at 6th carbon from the methyl end. Linolenic acid ($C_{18}H_{30}O_2$) contains three double bonds where the first double bonds is placed at 3th carbon from the methyl end. CH_3 (methyl protons), CH_2 (bulk methylene protons), CH = CH – **C*H*$_2$** – (allylic protons, i.e. – **C*H*$_2$** –, attached to a group of CH = CH), – CH = CH– **C*H*$_2$** – CH = CH – (diallylic methylene protons, i.e. – **C*H*$_2$** –, attached to between two double bounds), and CH = CH (olefinic protons) peaks are located at ~ 0.9 ppm, ~ 1.3 ppm, ~ 2.1 ppm, ~ 2.8 ppm, and ~ 5.35 ppm, respectively, in a proton MRS spectrum as shown in Figure 2.3.

Figure 2.2 shows unsaturated fatty acids: oleic acid, linoleic acid, and linolenic acid, which are found in edible oils. In chemical terms, oleic acid (CH_3 – $(CH_2)_7$ – CH = CH – $(CH_2)_7$ – COOH) is the representative of MUFA (e.g. monounsaturated omega–9, $\omega-9$, or n–9 fatty acid, which contains only one double bound that is placed at the 9th carbon from the methyl (CH_3) end). PUFA can be primarily divided into two groups: linoleic acid (CH_3 – $(CH_2)_4$ – CH = CH – CH_2 – CH = CH – $(CH_2)_7$ – COOH) , and linolenic acid (CH_3 – CH_2 – CH = CH – CH_2 – CH = CH

– CH_2 – CH = CH – $(CH_2)_7$ – COOH). A linoleic acid represents diaunsaturated $\omega-6$ or n–6 FA that refers to two double bonds where the first double bonds is placed at 6th carbon from the methyl end. A linolenic acid represents triunsaturated $\omega-3$ or n–3 FA that has three double bonds where the first double bonds is located at the 3rd carbon from the methyl end, as shown in Figure 2.2.

Figure 2.3 shows a spectrum obtained from corn oil. Methyl (CH_3), bulk methylene (CH_2), allylic (CH = CH – CH_2 –), diallylic methylene (= CH – CH_2 – CH =), and olefinic (CH = CH) protons in Figure 2.2 are labelled. The methyl, methylene, allylic, diallylic, and olefinic peaks are located at ~ 0.9 ppm, ~ 1.3 ppm, ~ 2.1 ppm, ~ 2.8 ppm, and ~ 5.35 ppm[4,5,6,7], respectively, as shown in Figure 2.3**.**

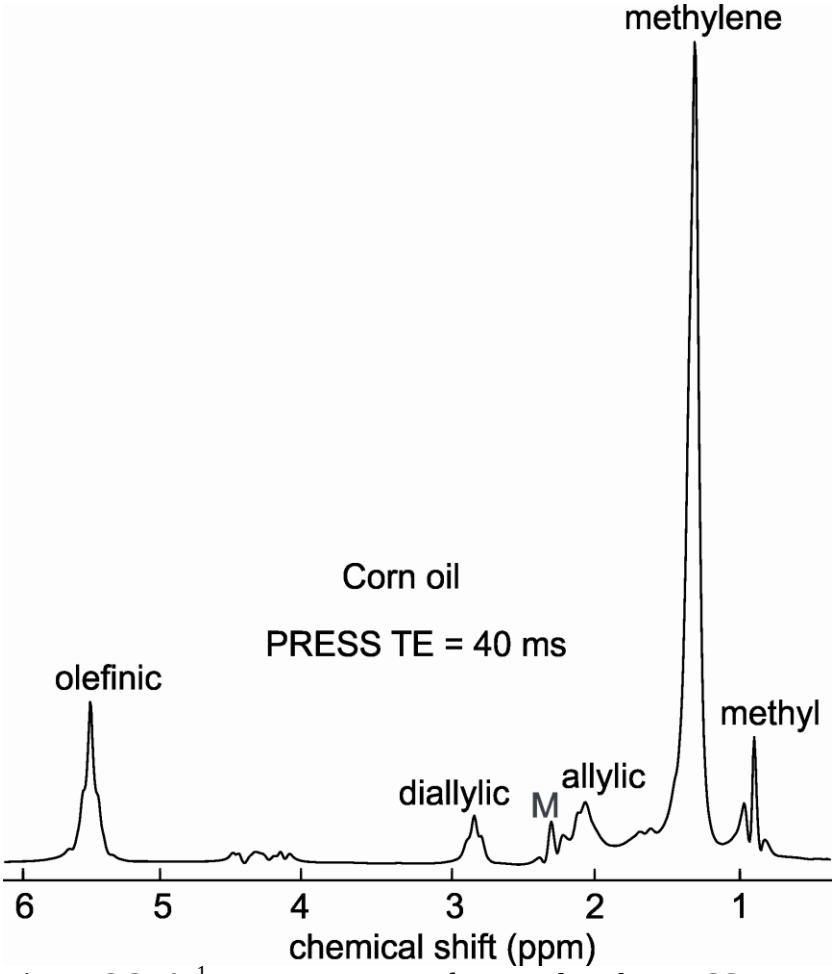

Figure 2.3. A ^{1}H MR spectrum of corn oil with PRESS TE = 40 ms at 3 T. The labeled peaks represent the molecular groups shown in Figure 2.2. Methyl (CH_3), methylene (CH_2), allylic (CH = CH–**C*H*$_2$**–), diallylic (= CH–**C*H*$_2$**–CH =), and olefinic (CH = CH) peaks are located at ~ 0.9 ppm, ~ 1.3 ppm, ~ 2.1 ppm, ~ 2.8 ppm, and ~ 5.35 ppm[4,5,6,7]. M is other methylene protons α to COO (–CH_2–COO) at ~ 2.25[4]. In this thesis, measurements of olefinic, and methylene peaks were only considered.

2.3 Relevance of Lipid Olefinic Protons

The olefinic protons are bonded to the carbon atoms which are linked together by double bonds and therefore they give a measure of lipid unsaturation. Levels of lipid unsaturation have been shown to be relevant to the study of breast cancer[8,9]. Lipid unsaturation levels in breast were determined by using MRS at 2.1 T with a selective multiple-quantum coherence transfer (Sel-MQC) technique[8], which is not readily available on a clinical MRI scanner. The outcome showed that unsaturation levels were lower in cancerous breast tissue compared to healthy breast tissue[8] (Ref.(8) speculates that the drop in unsaturation levels may be due to lower fat content in the tumour tissue because of loss of healthy cells in the abnormal tissue). Another study, which used ^{1}H-MRS at 7 T to detect normal nodes and abnormal nodes of breast cancer patients, showed that metastatic lymph nodes due to breast cancer yielded lower unsaturation levels compared to benign nodes[9]. Using ^{1}H MRS, the olefinic proton peak (– CH = CH –), which resonates at ~ 5.4 ppm , yields a measure of lipid unsaturation.

2.4 J-Coupling of Olefinic Protons

Figure 2.4 displays a portion of a fatty acid that contains the olefinic, allylic and diallylic (i.e. methylene protons) protons. The olefinic protons resonate at ~ 5.4 ppm and are bonded to the two carbon atoms that bind to each other with double bonds. The allylic, and diallylic protons neighbor the olefinic protons, and resonate at ~ 2.1 and ~ 2.8 ppm, respectively. The olefinic protons are J-coupled to their neighboring protons and to each other (Figure 2.4). J_2 is a coupling constant between the two olefinic protons, and is in the range of 11.3 - 16.3 Hz[10]. J_1 and J_3 are coupling constants between the olefinic protons to their neighbouring methylene protons. J_1-coupling constant is the same as J_3-coupling constant which is ~ 7 Hz[10]. In addition, the chemical shift difference between the two olefinic protons ($\delta_{olefinic}$) is ~ 0.5 ppm[10]. If J_2 is taken as 16.3

Hz, the ratio of $\frac{J_2}{\delta_{olefinic}} \cong 0.225$ at 3 T, which is more than twice the ratio of $\frac{J}{\delta} \cong 0.1$, which is considered to be a threshold for weak–coupling[11]. Therefore, the olefinic protons are strongly coupled to each other as has been assumed to be the case at 1.5 T[5,12]. As discussed in chapter 1, the splitting pattern for strongly-coupled spins is more difficult to predict as is their response to pulse sequences. On the other hand, the ratios of $\frac{J_1}{\delta_{olefinic-diallylic}} \approx 0.021$, and $\frac{J_3}{\delta_{olefinic-allylic}} \approx 0.017$ at 3 T are about five and six times smaller than 0.1. Therefore, the olefinic protons are weakly coupled to neighbouring methylene protons.

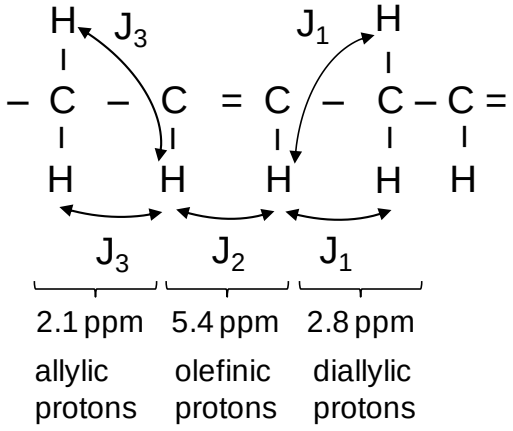

Figure 2.4. J-coupling of olefinic protons. Olefinic, allylic and diallylic protons resonate at ~ 5.4, ~ 2.1, and ~ 2.8 ppm, respectively. J_2 is a coupling constant between the two olefinic protons. J_1 and J_3 are coupling constants between the olefinic protons to their neighbouring methylene protons (i.e. diallylic (–CH=CH–**C*H*$_2$**–CH=CH–), and allylic (–**C*H*$_2$**–CH=CH) protons, respectively).

2.5 Previous Studies for Optimizing Measurement of Olefinic Protons *In-Vivo* by ^{1}H MRS

In Figure 2.3, the olefinic peak is clearly visible; however, in anatomical regions such as liver, and spinal bone marrow the peak is obscured by the large water resonance at ~ 4.7 ppm. Therefore, short-TE methods are not suitable for its quantification. Lundbom et al.[13,14,21] optimized a PRESS sequence, and found a long TE of 200 ms to be suitable for olefinic signal measurement at 1.5 T. The long TE enabled the water peak to decay by T_2 relaxation. In addition to this study, PRESS was also recently optimized by Troitskaia et al.[15] for measuring the olefinic resonance at 3 T by employing a TE of 200 ms. Both studies at 1.5 T and 3 T showed that the olefinic peak was well resolved from water peak at TE = 200 ms in liver and spinal bone marrow, respectively. In addition, at both field strengths, the olefinic peak signal losses due to J – coupling were minimized when TE = 200 ms. However, a TE of 200 ms is relatively long and results in significant T_2 signal loss *in-vivo*. For example, a T_2 of 70 ms results in ~ 94% signal loss when TE = 200 ms assuming a monoexponential decay $\exp(-TE/T_2)$.

2.6 Thesis Objective – Investigating Response of Olefinic Protons to STEAM

STEAM inherently suppresses 50% of signal from uncoupled spins such as water. Therefore, it could potentially provide a TE that is significantly shorter than 200 ms at which the olefinic protons are well resolved from water. The objective of this thesis work is to examine the response of lipid olefinic protons to a STEAM sequence to determine whether an optimal long – TE exists that yields higher olefinic signal *in-vivo* compared to a PRESS TE = 200 ms sequence. To our knowledge, the response of olefinic protons to STEAM has not been previously investigated for TE values longer than 60 ms[16].

2.7 Experimental Set-Up for Phantom Measurements

The response of lipid olefinic protons to a standard STEAM pulse sequence was examined in this thesis. To obtain optimal STEAM mixing time (TM), and echo time (TE) values, measurements of nine edible oils (almond, canola, cod liver, corn, linseed, peanut, sesame, sunflower, and walnut) were employed. Figure 2. 5 shows the experimental set-up for phantom measurements. All phantom experiments were carried out with a 3 T whole body MRI scanner (Intera, Philips Healthcare, Best Netherlands). A transmit/receive radiofrequency (RF) head coil (Philips Healthcare) was used. The head birdcage coil was placed on the patient table and oil phantoms were centred within the coil. Next, the patient table was advanced into the magnet, such that the phantom was centred in the magnet (with the aid of a positioning laser).

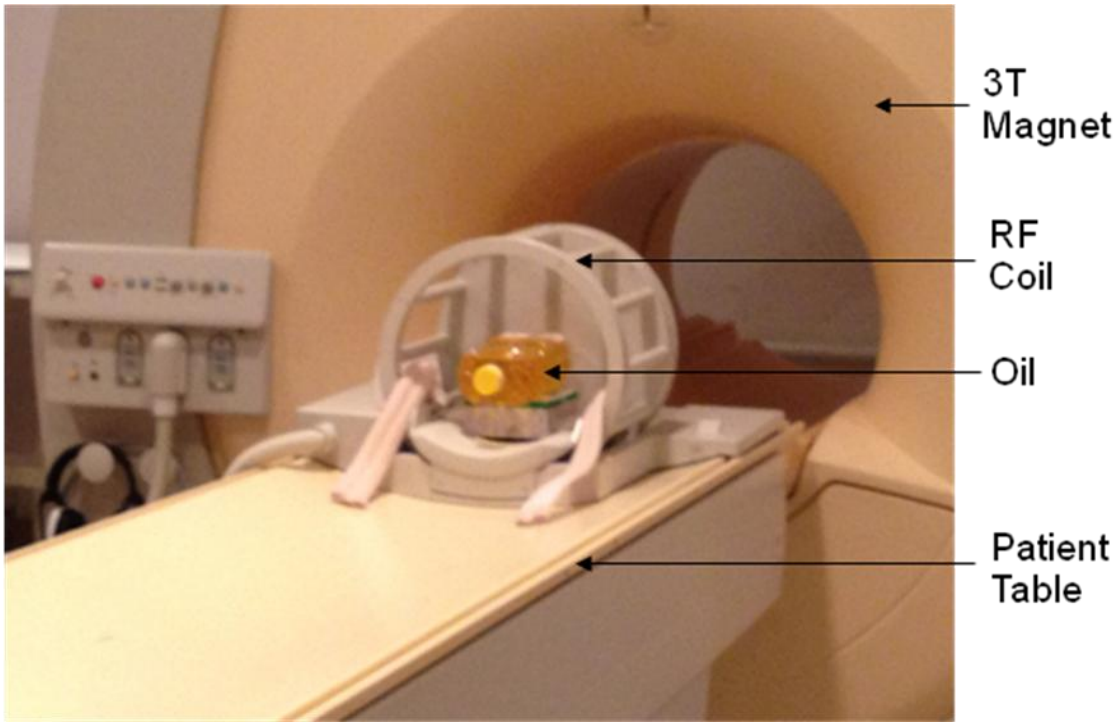

Figure 2. 5. Experimental set-up for phantom measurements.

Scout images were acquired. The PRESS or STEAM MRS voxel was positioned in the centre of the phantom based on the scout images. The following parameters were used for these localization techniques: mixing time (TM) = 20 ms (optimal STEAM TM that was determined, and is discussed in chapter 3), repetition time (TR) = 3 s, volume of interest (VOI) = 2 x 2 x 2 cm^3 or 1 x 1 x 1 cm^3, and number of signal averages (NSA) = 32 or 64, number of samples = 2048, spectral bandwidth = 2000 Hz. No water suppression was required and a 16 step phase-cycling scheme was applied. The RF pulse frequency offset was set 3.35 ppm (mean of methylene and olefinic chemical shifts) for the oils ($\frac{5.4+1.3}{2} \cong 3.35\,ppm$). Since the PRESS 180^o pulse bandwidth (1263 Hz) and STEAM pulse bandwidth (1967 Hz) were 9.88 ppm and 15.55 ppm, respectively, at 3 T, and both bandwidths' values are larger than the chemical shift difference of 5.4 – 1.3 ppm = 4.1 ppm, the choice of resonance chemical shift displacement effects in the homogeneous phantoms were not significant. Therefore, the exact frequency offset was not very critical; however, for consistency of results we took care to ensure that the frequency offset was at the central chemical shift.

2.8 Phantom Data Analysis

For post-processing, a Philips spectroscopy processing software was used for all spectra. Acquired MRS spectra are initially incorrectly phased due to phase difference between the magnetization and the receiver[18]. Figure 2.6 shows a ^{1}H MR spectrum after filtering and Fourier transformation of a corn oil spectrum obtained with PRESS TE = 40 ms at 3 T before applying phase correction. To quantify peak areas, heights, and widths, the spectrum needs to be phase corrected. To describe a phase correction, generally an adjustable phase angle (ϕ_c) is given by[19] the following equation: $\phi_c = \phi_0 + (\omega_0 - \omega)\phi_1$, where ϕ_0 and ϕ_1 are the zero and the first order

phase corrections, respectively, and ω is the resonance frequency of each individual resonance. Since chemical shift evolutions were refocused in our PRESS and STEAM experiments only a zero order phase correction was applied. The zero order phase correction is necessary to compensate for the phase which arises because of the detection process. Therefore, a phase correction was applied to all acquired spectra to get an in-phase spectrum (Figure 2.3) by using the Philips spectroscopy processing software. Phase correction of the spectrum was manually made with respect to methylene peak because the methylene peak does not suffer from the phase modulations that other peaks do due to J-coupling. Next, the methylene peak position was set to 1.3 ppm. Once phase corrected, and peak positions were assigned, the standard deviation of the noise was also recorded for all spectra between 8 ppm and 12 ppm. Finally, a baseline correction was made. The point of using a baseline correction is to remove variation (i.e. nearly constant background) from the baseline spectrum so to obtain a more smooth baseline of the spectrum that may improve the spectrum outcome quantifications (e.g. peak heights, widths and areas) when the best spectrum fitting is acquired. A polynomial function is employed for the baseline fitting, such as $a_3\delta^3 + a_2\delta^2 + a_1\delta + a_0$ where a_i is variables that are adjusted for the best spectrum fit, and δ is chemical shift (or frequency) along the horizontal direction of the spectrum (i.e. position of the spectrum).

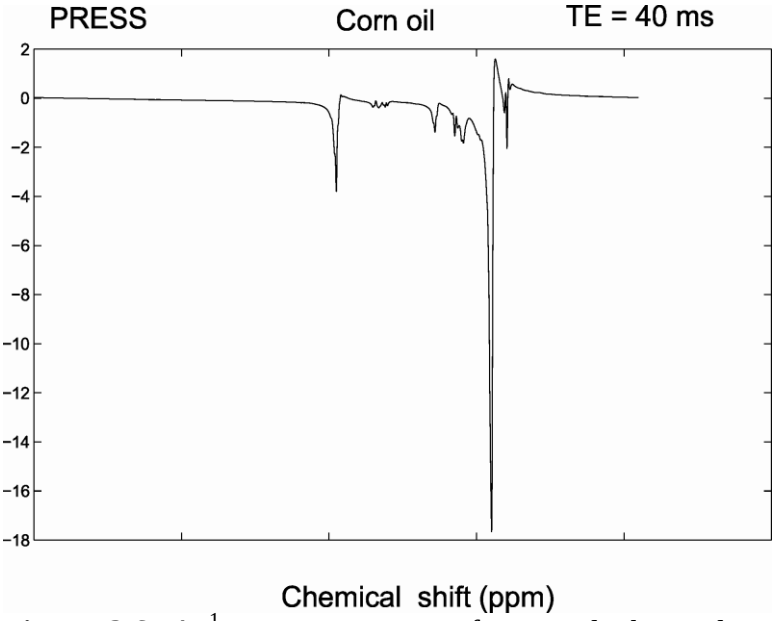

Figure 2.6. A ^{1}H MR spectrum of corn oil obtained with PRESS TE = 40 ms at 3 T before applying a phase correction.

Resonance areas of the 1.3 ppm methylene and 5.35 ppm olefinic peaks were measured using the Philips spectroscopy processing software that gave a table about the peaks of interest, including the peak areas, heights, widths, noise, and SNR for all spectra. The software allows to make a measurement on any region of interest on the peak, and then provides the output table respect to that region of interest. The methylene peak areas were measured between 1.08 and 1.53 ppm, and the olefinic peak areas were measured between 5.16 and 5.51 ppm, as shown in Figure 2.7. To give an idea of the SNR of the oil spectra, the olefinic peak height (i.e. peak signal) and the standard deviation of the noise in the same spectrum were about 1.46674 and 0.00069, respectively, for the walnut oil with STEAM TE = 100 ms. Thus, SNR (i.e. SNR = Signal/Noise) for the olefinic resonance for the walnut oil was calculated to be 2125.71. The noise was within ± 2% for all oil measurements (acquired with the same number of averages).

Figure 2. 8 shows the response of the methylene protons of the oils to STEAM as a function of TE. The signal decays monotonically with increasing TE because there are minimal losses due to J-coupling. Therefore, the methylene peak is a suitable phase correction and normalization reference. The response of olefinic protons of all oils to the STEAM sequence is discussed in chapter 3. As will be seen in chapter 3, the response of the olefinic protons to STEAM as a function of TE (TM = 20 ms) exhibits very small local maxima. To verify that the data points are actually local maxima and not due to reproducibility errors, ten STEAM spectra (TM = 20 ms) were acquired from the walnut oil phantom with each of TE = 90, 100, 110, 120, 130, 140, 150 and 160 ms (total of 80 spectra). The mean and standard deviation of the olefinic peak area over the ten spectra for each TE were calculated. The coefficient of variation (standard deviation/mean) for each TE was less than 0.75%. The error bar would be barely visible on the measurements if this small value is plotted.

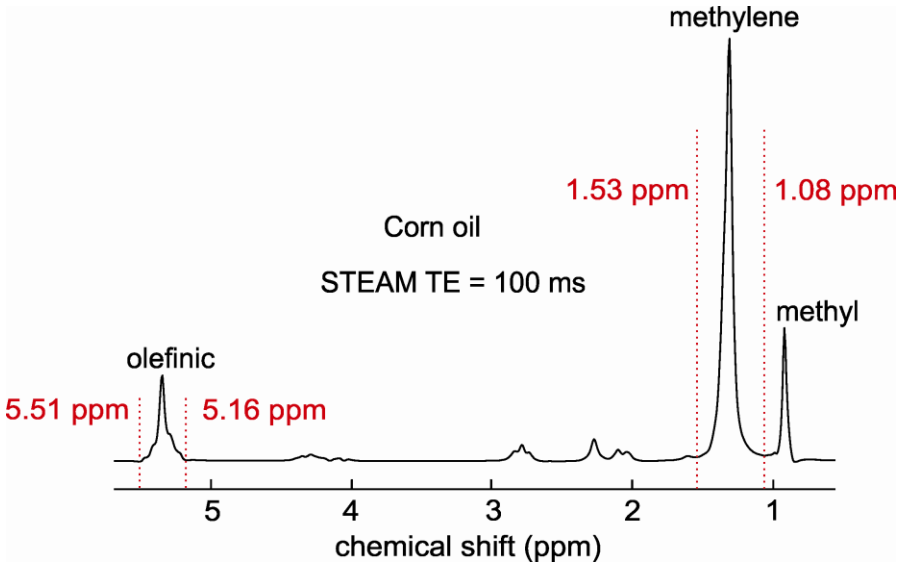

Figure 2.7. A proton MR spectrum of corn oil with STEAM (TE = 100 ms, and TM = 20 ms) at 3 T. Two cursors were separately placed on both sides of the methyelene, and olefinic peaks to obtain their integrals. In this study, measurements of olefinic, and methylene peaks were only considered.

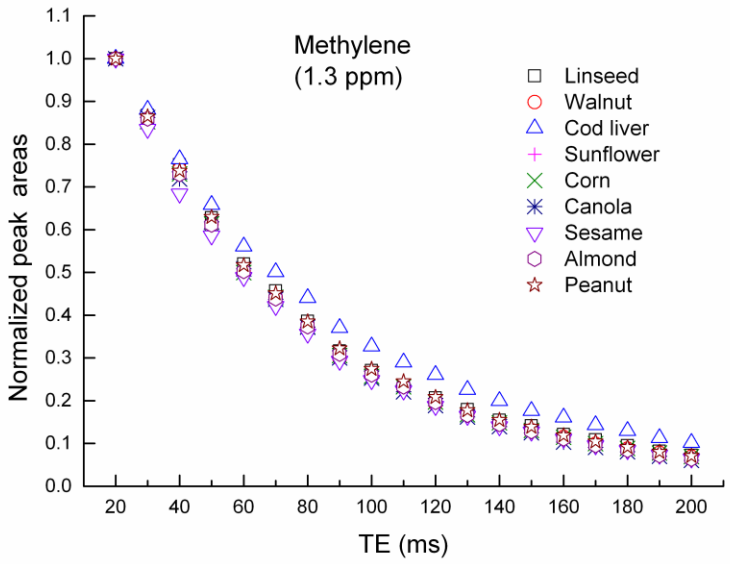

Figure 2. 8. Normalized peak areas of the methylene protons of the nine edible oils listed on the plot to STEAM as a function of TE.

2.9 Compositions of Fatty Acids

Compositions of nine edible oils were determined from literature and from the composition an estimate was obtained from the ratio of the number of olefinic protons to metylene protons as shown in Table 2.1. Each oil listed in Table 2.1 consists of different percentages of saturated fatty acids (SFA), and unsaturated fatty acids (UFA) (mainly oleic, linoleic, and linolenic acids). Mean values of oil compositions were considered when they were determined from more than one source/reference. As given in Table 2.1, the number of methylene protons in oleic, linoleic, and linolenic acid is 20, 14, and 8, respectively. The number of olefinic protons present in the oleic, linoleic, and linolenic acid is 2, 4, and 6, respectively. Saturated fatty acids contain zero olefinic protons, and the number of methylene protons for SFA in each oil depends on the different SFA constituents (e.g. sesame oil contains 6.7%[24] stearic

acid, and 9.6%[24] palmitic acid while corn oil contains 2%[23] stearic and 11%[23] palmitic acid). There was no contribution of eicosapentaenoic acid (EPA), docosapentaenoic acid (DPA), and docosahexaenoic acid (DHA) to the eight edible oils listed in Table 2.1. Finally, the ratio of number of olefinic protons to methylene protons was computed for each oil (Table 2.1). For example, for almond oil,

$$\frac{\#\,of\ olefinic\ protons}{\#\,of\ methylene\ protons}=\frac{2\times 0.6159+4\times 0.2921+6\times 0.001}{29\times 0.0909+20\times 0.6159+14\times 0.2921+8\times 0.001}=0.126\,.$$

In addition, the composition of cod liver oil was also determined from the literature. 21.8% of cod liver oil composition is polyunsaturated fatty acids (PUFA) (mainly EPA, DPA, and DHA). Since this extra contribution is significant, all have to be taken into account. The ratio of the number of olefinic protons to methylene protons, like the other oils, was computed as shown in Table 2.2.

Table 2.1. Compositions of the edible oils were determined from literature. The ratio of number of olefinic protons to methylene protons was computed for each oil.

Oil	SFA	Oleic Acid	Linoleic Acid	Linolenic Acid	$\frac{\#\ of\ olefinic\ protons}{\#\ of\ methylene\ protons}$
Almond[20] (%)	9.09	61.59	29.21	0.1	0.126
# of methylene protons/molecule	29	20	14	8	
# of olefinic protons/molecule	0	2	4	6	
Canola[21,22] (%)	7	62.3	20.55	9.15	0.146
# of methylene protons/molecule	26	20	14	8	
# of olefinic protons/molecule	0	2	4	6	
Corn[22,23] (%)	13.2	31.5	52.85	1	0.160
# of methylene protons/molecule	28	20	14	8	
# of olefinic protons/molecule	0	2	4	6	
Linseed[21,22,24,25] (%)	9.13	18.41	15.38	56.79	0.342
# of methylene protons/molecule	27	20	14	8	
# of olefinic protons/molecule	0	2	4	6	
Peanut[21,22,24] (%)	15.8	49.27	30.06	0.03	0.120
# of methylene protons/molecule	26	20	14	8	
# of olefinic protons/molecule	0	2	4	6	
Sesame[21,22,24] (%)	15.6	42.27	41.63	0.3	0.136
# of methylene protons/molecule	27	20	14	8	
# of olefinic protons/molecule	0	2	4	6	
Sunflower[21,22,26] (%)	11.5	29.66	58.12	0.1	0.170
# of methylene protons/molecule	27	20	14	8	
# of olefinic protons/molecule	0	2	4	6	
Walnut[21] (%)	12.3	4	70.2	13.6	0.248
# of methylene protons/molecule	26	20	14	8	
# of olefinic protons/molecule	0	2	4	6	

Table 2.2. Composition of cod liver oil was determined from literature. Cod liver also contains eicosapentaenoic acid (EPA), docosapentaenoic acid (DPA), docosahexaenoic acid (DHA), which are types of PUFA.

Oil	SFA	Oleic Acid	Linoleic Acid	Linolenic Acid	EPA	DPA	DHA	$\frac{\#\ of\ olefinic\ protons}{\#\ of\ methylene\ protons}$
Cod liver[21] (%)	22.5	51.8	2.7	1.1	9.9	1.2	10.7	0.215
$\frac{\#\ of\ methylene\ protons}{molecule}$	26	20	14	8	0	4	0	
$\frac{\#\ of\ olefinic\ protons}{molecule}$	0	2	4	6	10	10	12	

After the optimal STEAM echo time, 100 ms, was found (measurements and outcomes are discussed in more detail in chapter 3), areas of methylene and olefinic peaks were measured for each oil at the optimal STEAM TE = 100 ms. The ratios of measured olefinic peak areas to the measured methylene peak areas were calculated for all nine oils from the optimal STEAM (TE =100 ms), and the optimal PRESS (TE = 200 ms) spectra, and then compared to the ratios of calculated number of olefinic protons to the calculated number of methylene protons from compositions in the literature estimates for almond[20], canola or rapeseed[21,22], cod liver[21], corn[22,23], linseed[21,22,24,25], peanut or groundnut[21,22,24], sesame[21,22,24], mid-oleic sunflower[21,22,26], and walnut oil[21]. The calculated number of olefinic/number of methylene protons ratios versus the measured olefinic/methylene peak area ratios were plotted to obtain a linear coefficient of determination, R^2.

Figure 2.9, and Figure 2.10 show that excellent linear correlations were obtained between the measured and calculated values for the olefinic/methylene ratios. The linear coefficient of determination, $R^2 = 0.974$, obtained from the optimal STEAM (TE = 100 ms) sequence is better

than the linear coefficient of determination, $R^2 = 0.923$, obtained from the optimal PRESS (TE = 200 ms) sequence. The R^2 confirmed the R^2 obtained in the previous study (0.924)[15], which optimized the PRESS TE for olefinic protons at 3T.

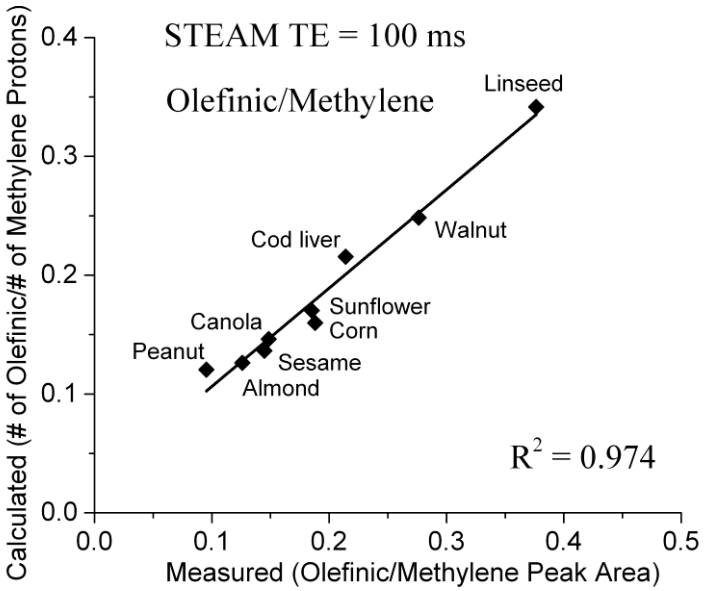

Figure 2.9. The ratio of olefinic to methylene peak areas measured with STEAM TE = 100 ms value exhibits an excellent linear correlation with the ratio of number of olefinic to number of methylene protons from the literature values estimates (the slope of the line is 0.829; y = 0.829x + 0.021). For the same oil, mean values of the calculated ratios were taken from the literature due to the variations in the compositions of those oils.

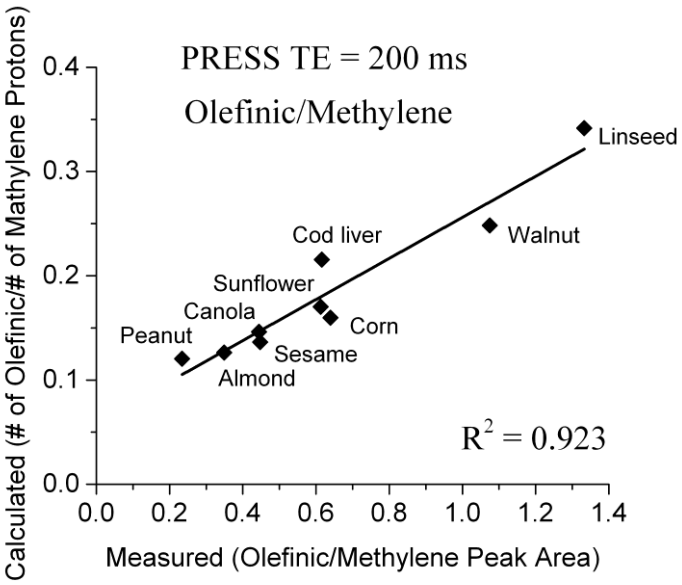

Figure 2.10. The ratio of olefinic to methylene peak areas measured with PRESS TE = 200 ms exhibits a good linear correlation with the ratio of number of olefinic to number of methylene protons from the literature values estimates (the slope of the line is 0.197; y = 0.197x + 0.059). For the same oil, mean values of the calculated ratios from the literature were employed due to the variations in the compositions of those oils.

2.10 *In-Vivo* Measurements

Measurements were also made *in-vivo* in spinal bone marrow to investigate the olefinic signal yield when using STEAM compared to PRESS. As shown in Figure 2.11, the olefinic proton peak (– CH = CH –) at ~ 5.35 ppm is obscured by the large water peak at ~ 4.75 ppm. This is especially a problem in regions of poor field homogeneity like spinal bone marrow because the poorer field homogeneity causes broader linewidths for the peaks causing them to overlap As a result, standard short-TE PRESS or STEAM sequences are not suitable for the olefinic peak's quantification as mentioned in section 2.5.

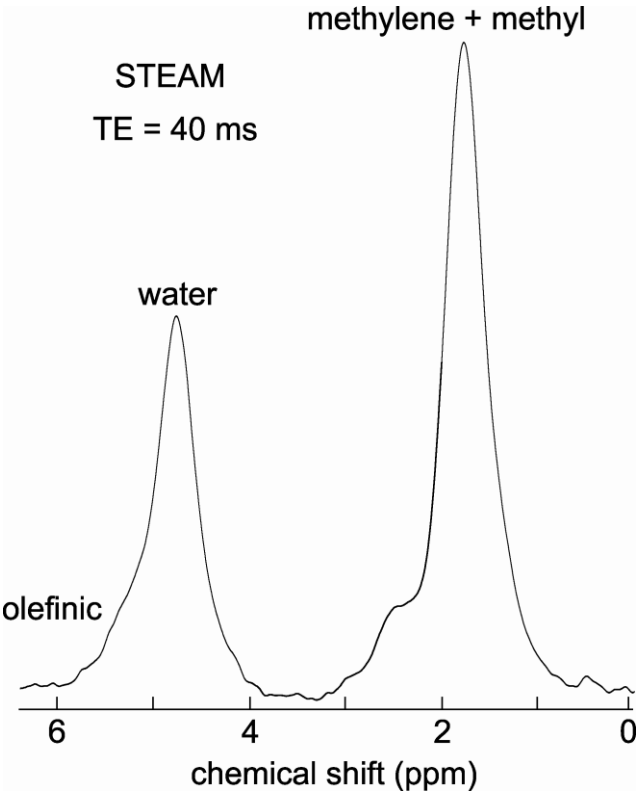

Figure 2.11. The spectrum acquired from vertebral spinal bone marrow of a healthy volunteer by using STEAM TE = 40 ms.

2.10.1 Measurements

For the *in-vivo* measurements, the scanner's built-in body coil was used for radiofrequency transmission, and a single element of a phased array surface coil (Sense-Flex-L, Philips Healthcare) was used for signal reception. The volunteer lay on a mattress positioned on the patient table over the surface coil. The volunteer was positioned such that the L4 vertebra was centred in the coil. A consent form was signed by each volunteer before scanning. The scan region of interest (L4 vertebra) was positioned in the magnet isocentre with the aid of the positioning laser. Sagittal, and axial T_1 weighted images were taken of the L4 vertebra. The images were used to localize the spectroscopy voxel accurately in two orthogonal views (transverse and sagittal) within the L4 vertebra. The following parameters were used for the

imaging scans: echo time (TE) = 8 ms, repetition time (TR) = 800 ms, reconstructed voxel size = 0.86 x 0.86 mm^2, slice thickness = 5 mm, field of view (FOV) = 220 x 220 x 50 mm^3, number of slice = 10 , and number of signal averages (NSA) = 1. The voxel was positioned in the center of the L4 vertebra, as shown in Figure 2.12.

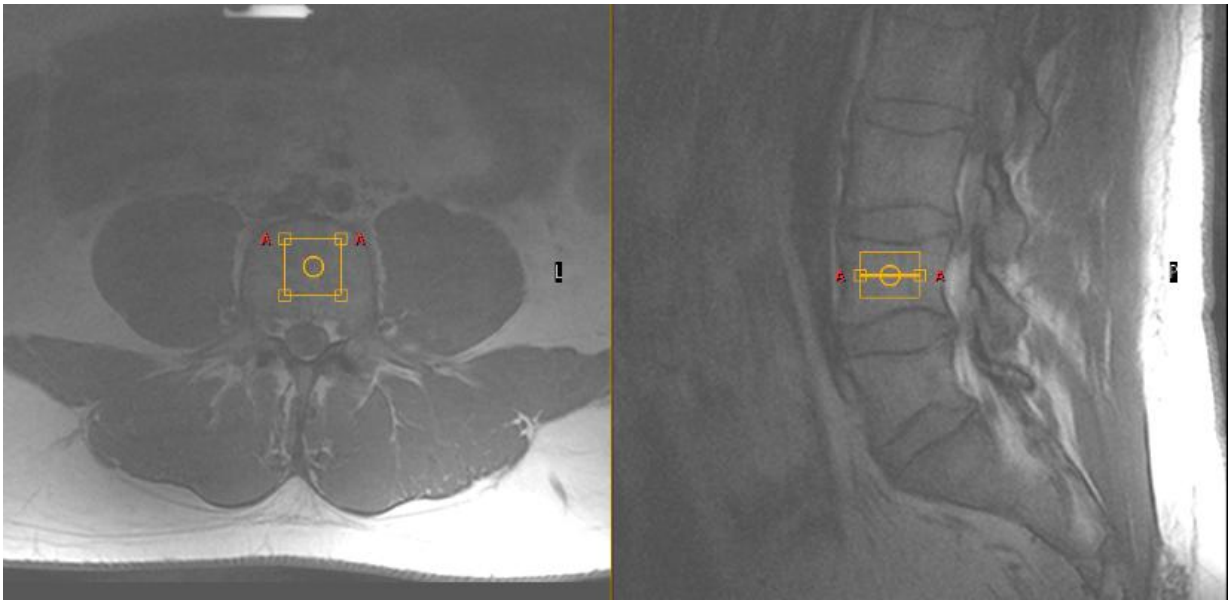

Figure 2.12. Axial (left) and sagittal (right) T_1-weighted images of spine of a healthy volunteer with the voxel placed in the L4 vertebra.

The following parameters were used for the PRESS and STEAM sequences for *in-vivo* scans: mixing time (TM) = 20 ms (for STEAM), repetition time (TR) = 3 s, volume of interest (VOI) = 2 x 2 x 1.5 cm^3, and number of signal averages (NSA) = 32 or 128, number of dummy scans (i.e. number of start-up acquisition) = 4, number of phase cycles = 16, number of samples = 2048, spectral bandwidth = 2000 Hz. PRESS TE = 40 ms and STEAM TE = 40 ms in 32 averages were acquired from all four volunteers. In addition, PRESS TE = 200 ms and STEAM TE 100 ms spectra were obtained in 128 averages. In one of the volunteers PRESS spectra were also acquired with TE values of 80 ms and 120 ms to confirm the T_2 value obtained in Ref. 15. No water suppression was applied because the olefinic peak would be affected due to its close

proximity to water. The RF pulse frequency offset was centred between the methylene and olefinic resonance frequencies.

2.10.2 *In-Vivo* Data Analysis

As discussed in phantom data analysis section, a Philips spectroscopy processing software was also used for all spectra obtained from *in-vivo* measurements for post-processing. Spectra were filtered, Fourier transformed and phase corrected. For each volunteer, the noise in the spectrum, and peak area, height, and width were recorded for the olefinic, methyl + methylene, and water. As shown in Figure 2.11, the methylene (1.3 ppm) and methyl (0.9 ppm) peaks appeared as one peak due to broader linewidths characteristic of spectra obtained from the spine. To give an idea of the SNR of *in-vivo* spectra acquired in 128 averages, with PRESS TE = 200 ms, the olefinic peak height in one volunteer was 0.355 and the noise was 0.0134 yielding an SNR of about 26.5. When comparing signal areas of the olefinic resonance obtained with PRESS and STEAM, it was verified that the noise of the spectra being compared were within ± 2 % of each other.

2.10.3 Peak Fitting

For the *in-vivo* data, a Philips peak fitting software was used for area quantification because the STEAM spectra exhibited a residual water signal that overlapped with the olefinic peak. As discussed in the 3T manual (Application Guide, Volume 4 - Spectroscopy by Philips), the Philips spectral fitting routine modelled each peak as a linear combination of a Gaussian and a Lorentzian function $[aG+bL]$, (where a is the Gaussian weight that is an input parameter, G is the Gaussian equation, b is the Lorentzian weight that is an input parameter, L is the Lorentzian equation). Fitting was performed with a nonlinear least squares iterative method based on the Marquart and Levenberg algorithm[27,28]. Positions of the olefinic (5.35 ppm), water (4.75 ppm),

and methylene + methyl peaks (1.3 ppm) were manually set in a fitting script of the software first so that centres of peak fitting for each of the three peaks would accurately match with those centers of the peak positions. For example, the sum of three peak widths' variables from Gaussian ($G_{i=1,2,3}$) and Lorentzian ($L_{i=1,2,3}$) functions are $[a_1G_1+b_1L_1]_1+[a_2G_2+b_2L_2]_2+[a_3G_3+b_3L_3]_3$, where $a_{i=1,2,3}$ *and* $b_{i=1,2,3}$ are Gaussian and Lorentzian percentage parameters for the first, second and third peaks, respectively. Once optimized peak widths, heights are determined, the peaks are finally fitted with the linear combination of the both Gaussian and Lorentzian lineshapes. So the total area under the linear combination of a lineshape is yielded separately for each of the three peaks.

Figure 2.13, and Figure 2.14 shows the outcome of the peak fitting routing for the STEAM TE = 100 ms and PRESS TE = 200 ms spectra for one volunteer. The software provided peak areas for the olefinic, water, and methylene + methyl peaks. The ratio of olefinic peak area to the methylene + methyl peak area was calculated for each volunteer for the STEAM TE = 100 ms and PRESS TE = 200 ms spectra.

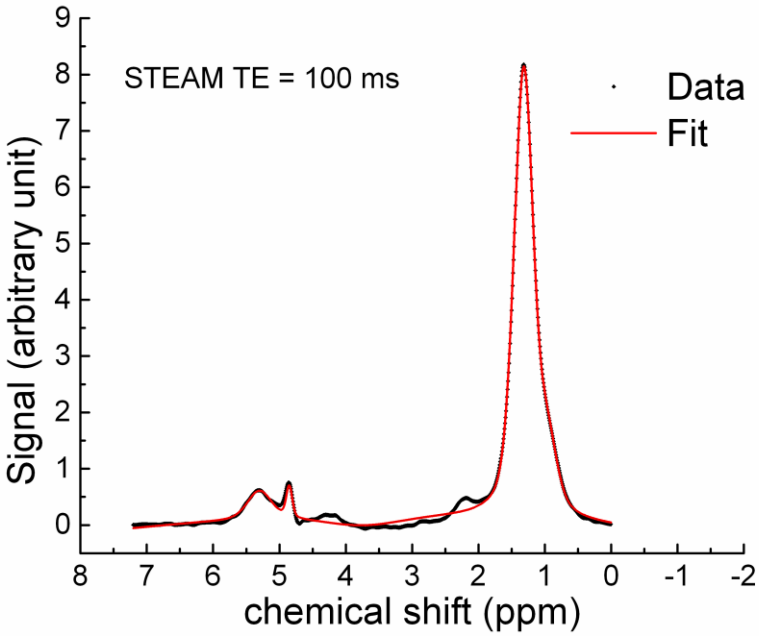

Figure 2.13. Peak fitting using the Philips automated spectroscopy software for STEAM TE = 100 ms. The olefinic (~ 5.35 ppm), water (~ 4.75 ppm), allylic (~ 2.1 ppm), and methylene + methyl peaks (~ 1.3 ppm) are visible from the L4 vertebra of a healthy volunteer scan.

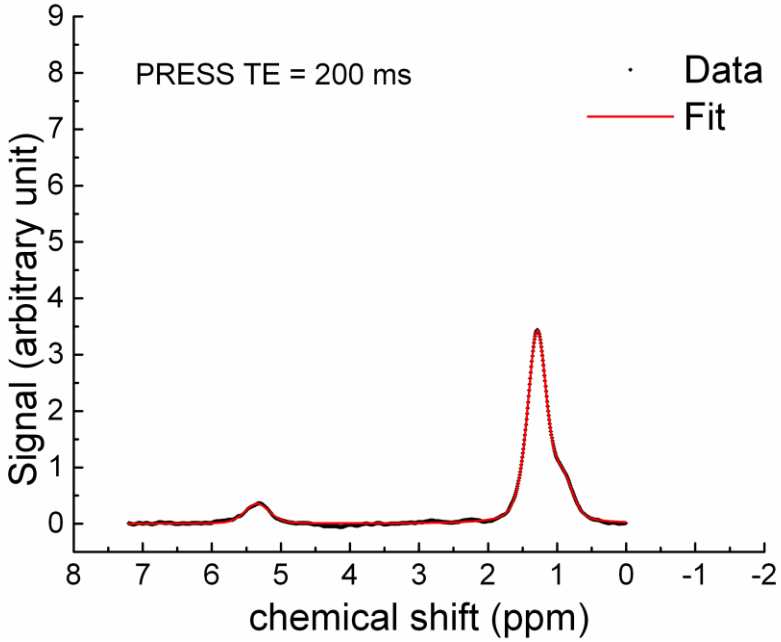

Figure 2.14. Peak fitting using the Philips automated spectroscopy software for PRESS TE = 200 ms. The olefinic (~ 5.35 ppm), and methylene + methyl peaks (~ 1.3 ppm) are displayed from the L4 vertebra of a healthy volunteer scan.

2.10.4 T_2 Value

Water T_2 value was estimated from the L4 vertebra bone marrow of a healthy volunteer scan from the PRESS TE = 40, 80 and 120 ms spectra. Equation (1.17) was linearized and an estimated T_2 of 20.2 ms was obtained, which agrees with a previous determined[15]. A T_2 value of 69.93 ms was also calculated for the methylene peak *in-vivo* from the same PRESS spectra used to calculate the water T_2 value. We are not aware of any T_2 values that have been reported for olefinic protons *in-vivo*.

2.10.5 Summary

Fatty acids, their characteristic NMR spectra, oil compositions, and the methods employed for *in-vitro* and *in-vivo* scans and for the data analysis were reviewed in this chapter. The outcomes of the investigations are given in the following chapter.

2.11 References

1. F. H. Martini, J. L. Nath, and E. F. Bartholomew. Fundamentals of Anatomy and Phyiology. 9th Ed., Pearson Education. Inc., San Francisco (2012).

2. E. Fahy et al. A comprehensive classification system for lipids. Journal of Lipids Research **46**, 839-861 (2005).

3. A. Barison, C. W. P. da Silva, F. R. Campos, F. Simonelli, C. A. Lenz, A. G. Ferreira. A simple methodology for the determination of fatty acid composition in edible oils through ^{1}H NMR spectroscopy. Magnetic Resonance in Chemistry **48**, 642-650 (2010).

4. J. Ren, I. Dimitrov, A. D. Sherry, C. R. Malloy. Composition of adipose tissue and marrow fat in humans by ^{1}H NMR at 7 Tesla. Journal of Lipid Research **49**, 2055-2062 (2008).

5. D. K. W. Yeung, J. F. Griffith, G. E. Antonio, F. K. H. Lee, J. Wood, and P. C. Leung. Osteoporosis is associated with increased marrow fat content and decreased marrow fat unsaturation: a proton MR spectroscopy study. Journal of Magnetic Resonance Imaging **22**, 279-285 (2005).

6. M. Oostendorp, U. F. H. Engelke, M. A. A. P. Willemsen, R. A. Wevers. Diagnosing inborn errors of lipid metabolism with proton nuclear magnetic resonance spectroscopy. Clinical Chemistry **52**, 1395-1405 (2006).

7. C. Fauhl, F. Reniero, C. Guillou. ^{1}H NMR as a tool for the analysis of mixtures of virgin olive oil with oils of different botanical origin. Magnetic Resonance in Chemistry **38**, 436-443 (2000).

8. Q. He, P. Shkarin, R. J. Hooley, D. R. Lannin, J. C. Weinreb, V. I. J. Bossuyt. In vivo MR spectroscopic imaging of polyunsaturated fatty acids (PUFA) in healthy and cancerous breast tissues by selective multiple quantum coherence transfer (Sel-MQC): A preliminary study. Magnetic Resonance in Medicine **58**, 1079-1085 (2007).

9. M. A. Korteweg, W. B. Veldhuis, W. Th. M. Mali, S. C. E. Diepstraten, P. R. Luijten, M. A. A. J. van den Bosch, R. M. J. C. Eijkemans, P. J. van Diest, D. W. J. Klomp. Investigation of lipid composition of dissected sentinel lymph nodes of breast cancer patients by 7 T proton MR spectroscopy. Journal of Magnetic Resonance Imaging **35**, 387-392 (2012).

10. J. M. Purcell, S. G. Morris, H. Susi. Proton magnetic resonance spectra of unsaturated fatty acids. Analytical Chemistry **38**, 588-592 (1966).

11. R. A. DE Graaf and D. L. Rothman. In vivo detection and quantification of scalar coupled ^{1}H NMR resonances. Concepts in Magnetic Resonance **13**, 32-76 (2001).

12. R. V. Mulkern, J. Meng, J. L. Bowers, K. Oshio, C. Zuo, H. Li, R. A. Kraft, D. S. Williamson, D. Jaramillo. In vivo bone marrow lipid characterization with line scan Carr-Purcell-Meiboon-Gill proton spectroscopic imaging. Magnetic Resonance Imaging **15**, 823-837 (1997).

13. J. Lundbom, A. Hakkarainen, S. Soderlund, J. Westerbacka, N. Lundbom, M-R. Taskinen. Long-TE ^{1}H MRS suggests that liver fat is more saturated than subcutaneous and visceral fat. NMR in Biomedicine **24**, 238-245 (2011).

14. J. Lundbom, A. Hakkarainen, B. Fielding, S. Soderlund, J. Westerbacka, M-R. Taskinen, N. Lundbom. Characterizing human adipose tissue lipids by long echo time ^{1}H-MRS in vivo at 1.5 Tesla: validation by gas chromatography. NMR in Biomedicine **23**, 466-472 (2010).

15. A. Troitskaia, B. G. Fallone, A. Yahya. Long echo time proton magnetic resonance spectroscopy for estimating relative measures of lipid unsaturation at 3 T. Journal of Magnetic Resonance Imaging **37**, 944-949 (2013).

16. G. Hamilton, M. S. Middleton, M. Bydder, T. Yokoo, J. B. Schwimmer, Y. Kono, H. M.Patton, J. E. Lavine, and C. B. Sirlin. Effect of PRESS and STEAM sequences on

magnetic resonance spectroscopic liver fat quantification. Journal of Magnetic Resonance Imaging **30**, 145-152 (2009).

17. M. I. Osorio-Garcia, A. R. C. Sava, D. M. Sima, F. U. Nielsen, U. Himmelreich and S. V. Huffel. Quantification Improvements of 1H MRS Signals, Magnetic Resonance Spectroscopy. Dong-Hyun Kim Ed., ISBN: 978-953-51-0065-2, InTech, Shanghai, China (2012).

18. L. Chen, Z. Weng, L. Y. Goh, L. M. Garland. An efficient algorithm for automatic phase correction of NMR spectra based on entropy minimization. Journal of Magnetic Resonance **158**, 164-168 (2002).

19. R. A. De Graaf. In vivo NMR spectroscopy. John Wiley & Sons Ltd, Baffins Lane, Chichester, England (2002).

20. M. Venkatachalam, S. K. Sathe. Chemical composition of selected edible nuts seeds. Journal of Agricultural and Food Chemistry **54**, 4705-4714 (2006).

21. J. Lundbom, S. Heikkinen, B. Fielding, A. Hakkarainen, M-R. Taskinen, N. Lundbom. PRESS echo time behavior of triglyceride resonance at 1.5 T: Detecting w-3 fatty acids in adipose tissue in vivo. Journal of Magnetic Resonance **201**, 39-47 (2009).

22. M. D. Guillen, A. Ruiz. Rapid simultaneous determination by proton NMR of unsaturation and composition of acyl groups in vegetable oils. Eur. J Lipid Sci. Technol. **105**, 688-696 (2003).

23. F. G. Dunlap, P. J. White, L. M. Pollak. Fatty acid composition of oil from exotic corn breeding materials. J Am Oil Chem Soc **72**, 989-993 (1995).

[24.] A. Kemal-Eldin, R. Andersson. A multivariate study of the correlation between tocopherol content and fatty acid composition in vegetable oils. J Am Oil Chem Soc **74**, 375-380 (1997).

[25.] M. Nykter, H-R. Kymäläinen, F. Gates, A-M. Sjoberg. Quality characteristics of edible linseed oil. Agricultural and Food Science **15**, 402-413 (2006).

[26.] I. Marekow, R. Tarandjiiska, S. Momchilova, B. Nikolova-Damyanova. Quantitative silver ion thin layer chromatography of triacylglycerols from sunflower oils differing in the level of linoleic acid. Journal of Liquid Chromatography and Related Technology **31**, 1959-1968 (2008).

[27.] K. Levenberg. A method for the solution of certain problems in least squares. Q Appl Math **2**, 164-168 (1944).

[28.] D. Marquardt. An algorithm for least-squares estimation of nonlinear parameters. SIAM J Appl Math **11**, 431-441 (1963).

Chapter 3 Comparison of Optimized Long Echo Time STEAM and PRESS Proton Magnetic Resonance Spectroscopy of Spinal Bone Marrow Lipid Olefinic Protons at 3 T*

3.1 Introduction

Proton magnetic resonance spectroscopy (MRS) measures of lipid unsaturation have shown to be relevant in the study of breast cancer[1,2], osteoporosis[3], obesity[4], and liver disease[5,6]. The olefinic peak at ≈ 5.3 - 5.4 ppm yields a measure of lipid unsaturation. However, at clinical field strengths, the olefinic resonance is largely overwhelmed by the water resonance at ≈ 4.7 ppm in certain anatomical regions such as spinal bone marrow and liver, rendering the standard *in-vivo* short-TE (echo time) PRESS (point resolved spectroscopy)[7] and STEAM (stimulated echo acquisition mode)[8] MRS pulse sequences not suitable for its observation. Therefore, long TE *in-vivo* MRS sequences have been investigated for measuring the olefinic resonance *in-vivo.* Previously, Lundbom *et al.* characterized the J-coupling (scalar coupling) evolution response of the lipid olefinic spins as a function of PRESS TE at 1.5 T[9] and determined that a PRESS sequence with a long TE of 200 ms was suitable for resolving the olefinic peak from water in liver at 1.5 T[10]. Recently, Troitskaia *et al.*[11] demonstrated that a PRESS sequence with a TE of 200 ms also reduced olefinic signal losses due to J-coupling evolution at 3 T. The optimized PRESS sequence was applied to spinal bone marrow and the long-TE resulted in almost complete suppression of the water signal due to the short transverse (T_2) relaxation (≈ 22 ms) time of water protons in vertebral bone marrow[11]. However, a TE of 200 ms results in significant T_2 decay of signal from the lipid protons themselves. For example, protons with T_2 constants less

*A version of this chapter has been accepted for publication.
A. Bingölbali, B.G. Fallone, A. Yahya, "Comparison of Optimized Long Echo Time STEAM and PRESS Proton Magnetic Resonance Spectroscopy of Lipid Olefinic Protons at 3 T", *Journal of Magnetic Resonance Imaging.*

than 100 ms will lose more than 85% of their signal when a TE of 200 ms is employed assuming a monoexponential decay. Thus the olefinic resonance may suffer from a poor signal to noise ratio (SNR) in pathological situations where levels of lipid unsaturation are reduced.

The STEAM sequence yields only 50% of the signal output of PRESS for uncoupled spins due to the nature of the stimulated echo[8,12], thereby inherently reducing the water signal significantly. Specifically in spinal bone marrow, assuming a water T_2 of 22 ms[12] at 3 T, the water signal should be diminished to less than 1% with a STEAM sequence with a TE of 90 ms. For J-coupled lipid spins such as the olefinic protons, it has been shown that the response to STEAM and PRESS differ due to differences in scalar coupling evolution during the two pulse sequences[13]. In this work, we investigate the J-modulation response of lipid olefinic protons to a STEAM sequence at 3 T. The objective is to determine an optimal long TE (TE ≥ 90 ms to sufficiently resolve the olefinic resonance from that of water) that minimizes J-coupling effects on the olefinic resonance but that is considerably shorter than 200 ms to reduce losses due to T_2 relaxation. The optimized long-TE STEAM sequence could serve as a better alternative to the optimized PRESS sequence (TE = 200 ms) in situations where SNR is critical. To our knowledge, the only other work that investigated the response of the olefinic protons to STEAM employed a maximum TE value of 60 ms[13]. The response of the olefinic protons of nine oils was examined as a function of STEAM TE. In addition, *in-vivo* measurements were performed on spinal bone marrow of healthy volunteers.

3.2 Materials and Methods

At 3 T, the olefinic protons are weakly coupled to neighbouring methylene protons (2.1 ppm allylic protons or 2.8 ppm diallylic protons) with a coupling constant of about 7 Hz and are strongly coupled to each other with a coupling constant in the range of 11.3 - 16.3 Hz[14]. All

phantoms and *in-vivo* experiments were carried out with a 3 T whole body MRI scanner (Intera, Philips Healthcare, Best, Netherlands). The scanner's automatic shimming procedure was employed for shimming and spectra were acquired as 2048 complex data points sampled at a frequency of 2000 Hz. The RF (radiofrequency) transmitter frequency was set to ≈ 3.35 ppm (centred between the 1.3 ppm methylene resonance and that of the 5.4 ppm olefinic protons).

For phantom experiments, a transmit/receive RF head coil (Philips Healthcare) was used. Measurements were performed on nine oils, namely, almond (Hain Celestial Canada ULC, Delta, BC, Canada), canola (No name, Loblaws, Canada), cod liver (Pharmetics, Laval, QC, Canada), corn (Canada Safeway, Calgary, AB, Canada), linseed (Sigma-Aldrich Canada, Oakville, ON, Canada), peanut (JVF Canada, Toronto, ON, Canada), sesame (Flavor Full Foods, Taipei Hsien, Taiwan), mid-oleic sunflower (Canada Safeway), and walnut (M. Graham, West Linn, OR, USA) oil. A standard STEAM pulse sequence was employed with the following parameters: repetition time (TR) = 3 s, volume of interest (VOI) = 2 x 2 x 2 cm^3 or 1 x 1 x 1 cm^3, and number of signal averages (NSA) = 32 or 64. No water suppression was required and a 16 step phase-cycling scheme was applied. The effect of mixing time (TM) on the response of the corn oil olefinic protons was first investigated. The STEAM sequence was run with TE values ranging from 20 to 200 ms in steps of 10 ms with TM fixed at 20, 25, 30, 35, 40, 45, 50, 75 or 100 ms. For the other phantom STEAM experiments, TM was fixed at 20 ms and nineteen TE values ranging from 20 to 200 ms in steps of 10 ms were employed to acquire spectra from all the oils. To ensure scan reproducibility ten STEAM spectra (TM = 20 ms) were also acquired from the walnut oil phantom with each of TE = 90, 100, 110, 120, 130, 140, 150 and 160 ms. A spectrum was also obtained from each of the oils with a PRESS sequence (same parameters as STEAM) with TE = 200 ms. In addition, a data set consisting of PRESS spectra with TE values ranging

from 40 to 240 ms in steps of 20 ms were measured from the corn oil phantom. For PRESS experiments, the first echo time (TE_1) was set to 20 ms and the total TE was changed by altering the second echo time (TE_2). Resonance areas of the 1.3 ppm methylene and 5.4 ppm olefinic peaks were determined for all spectra after they were manually processed using a Philips spectroscopy processing software.

The oils are composed of saturated (mainly myristic, palmitic, and stearic) and unsaturated fatty acids. The latter includes monounsaturated oleic acid, diunsaturated linoleic acid, and triunsaturated linolenic acid[15]. For each oil, the number of methylene and olefinic protons were estimated from oil compositions in the literature based on assumptions outlined in Ref.[11]. The ratio of the measured olefinic peak area to the measured 1.3 ppm methylene peak area was calculated for each of the oils and compared to the calculated ratio of the number of olefinic protons to the number of 1.3 ppm methylene protons obtained from literature estimates. The calculated ratios were plotted against the measured ratios for each of the oils to obtain a linear coefficient of determination, R^2.

For *in-vivo* scans, a single element of a phased array surface coil (Sense-Flex-L, Philips Healthcare) was responsible for signal reception while the scanner's built-in body coil was employed for RF transmission. Spectra were acquired from four healthy male volunteers of 27-38 years of age after they signed informed consent. For each volunteer, a voxel with dimensions of 2 x 2 x 1.5 cm^3 was placed in the L4 vertabra and spectra were obtained with both PRESS and STEAM. PRESS spectra were measured with TE values of 40 ms and 200 ms; a STEAM spectrum with TE = 100 ms was also obtained. For three of the volunteers, all spectra were acquired with 128 averages with the exception of the PRESS TE = 40 ms spectrum, which was measured with 32 averages. For the fourth volunteer 64 averages were employed instead of 128

due to time constraints. A TR of 3 s was used for all spectroscopy scans and TM was set to 20 ms for STEAM (the minimum obtainable TM when the body coil is used for excitation is 18 ms). Spectra were processed and phase corrected and then peak fitted using a Philips automated spectroscopy software. The methylene and methyl (0.9 ppm) peaks appeared as one peak due to broader linewidths characteristic of spectra obtained from the spine. The average linewidth of the collective peak over all the volunteers was measured to be ≈ 54 Hz from the PRESS TE = 40 ms spectra. The Philips spectral fitting routine modelled each peak as a linear combination of a Gaussian and a Lorentzian function. Fitting was performed with a nonlinear least squares iterative method based on the Marquart and Levenberg algorithm[16,17]. The software yielded peak areas for the olefinic and methylene + methyl peaks. The ratio of the olefinic peak area to the methylene + methyl peak area was calculated for each volunteer from the STEAM TE = 100 ms and PRESS TE = 200 ms spectra.

3.3 Results

The effect of changing TM on the corn oil olefinic peak area was investigated for a range of TE values. It was found that for TE values of 100 ms and 110 ms, a mixing time of 20 ms and 35 ms yielded the highest olefinic peak area whereas for all higher TE values, a TM of 20 ms yielded the highest area. Therefore, it was decided to employ a TM of 20 ms. Figure 3.1(a) displays as examples the normalized olefinic peak areas with varying STEAM TE for three different mixing times. Figure 3.1(b) shows the response of the olefinic protons of nine oils as a function of STEAM TE (TM = 20 ms); for a clearer presentation of the trend, the walnut oil data points are displayed separately in Figure 3.1(c). From the walnut oil reproducibility scans the mean and standard deviations of the olefinic peak areas over the ten spectra for each TE were calculated. The coefficient of variation (standard deviation/mean) for each TE was less than

0.75%. Figure 3.2(a) shows the spectral lineshapes of the walnut olefinic resonance for TE values ranging from 20 ms to 150 ms. Similar spectral lineshapes were obtained for all the oils at each TE. Figure 3.2(b) demonstrates the difference in response of the corn oil olefinic protons to PRESS and STEAM as TE is increased. Unlike with PRESS where J-modulation effects are clearly visible, the response to STEAM decreases monontonically with increasing TE except for small local maxima at TE values of 100 ms, 120 ms and 150 ms. Furthermore, as seen in Figure 3.2(c) the PRESS spectra exhibit negative multiplets whereas the STEAM spectra appear to be mostly in phase for TE values of 100 ms and higher. An optimal long TE of 100 ms was selected for observing the olefinic protons with STEAM because all the oils exhibited maximum olefinic area in the TE = 90 - 100 ms vicinity. The ratio of measured olefinic/methylene peak area was computed for all nine oils from the STEAM TE = 100 ms spectra and the measured results were compared with average values of the ratio of the number of olefinic to methylene protons determined from oil compositions in the literature[11] as shown in Figure 3.3. Measured olefinic/methylene peak area ratios exhibit an excellent linear correlation with the literature values estimates (R^2 = 0.975). The R^2 value of 0.975 is better than that previously determined (R^2 = 0.92) with PRESS TE = 200 ms spectra[11]. The R^2 of 0.92 for PRESS was also confirmed in this work. Averaged over all the oils, the olefinic signal area obtained with the STEAM TE = 100 ms was about 85% of that obtained with PRESS with TE = 200 ms.

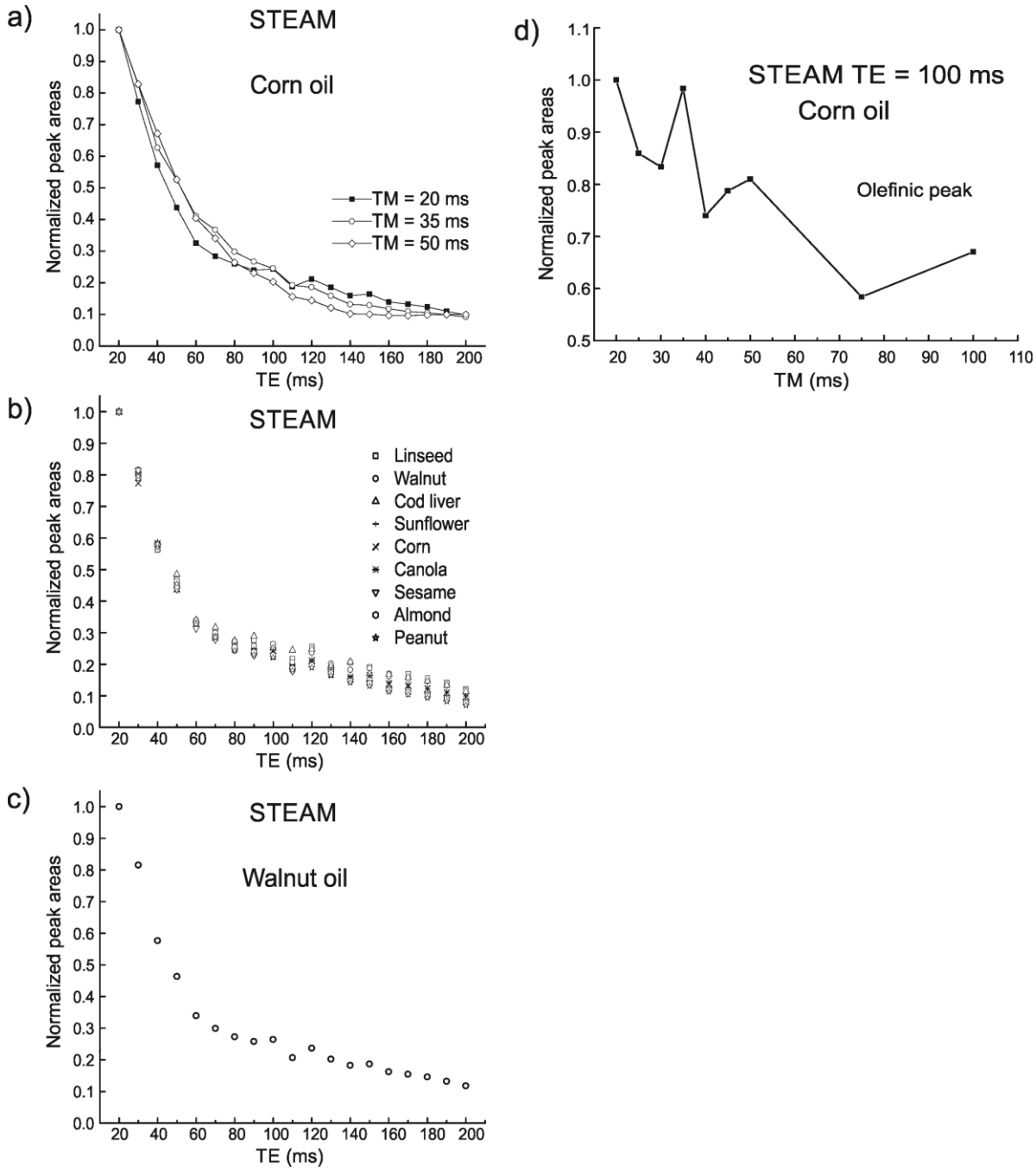

Figure 3.1. Olefinic peak areas plotted against STEAM TE. All areas are normalized to the area obtained with the shortest TE (20 ms). Panel (a) displays the corn oil olefinic peak areas as a function of STEAM TE for three different mixing times (20, 35 and 50 ms) while panel (b) shows the olefinic peak areas of the nine oils as a function of STEAM TE when TM = 20 ms. The plot in (c) isolates the walnut oil graph of (b) for the purposes of clarity. Small local maxima can be seen at TE values of 100, 120 and 150 ms. Also the plot in (d) shows the olefinic peak areas of the corn oil as a function of STEAM TM when TE = 100 ms. The signal doesn't monotonically decrease with increasing TM**.**

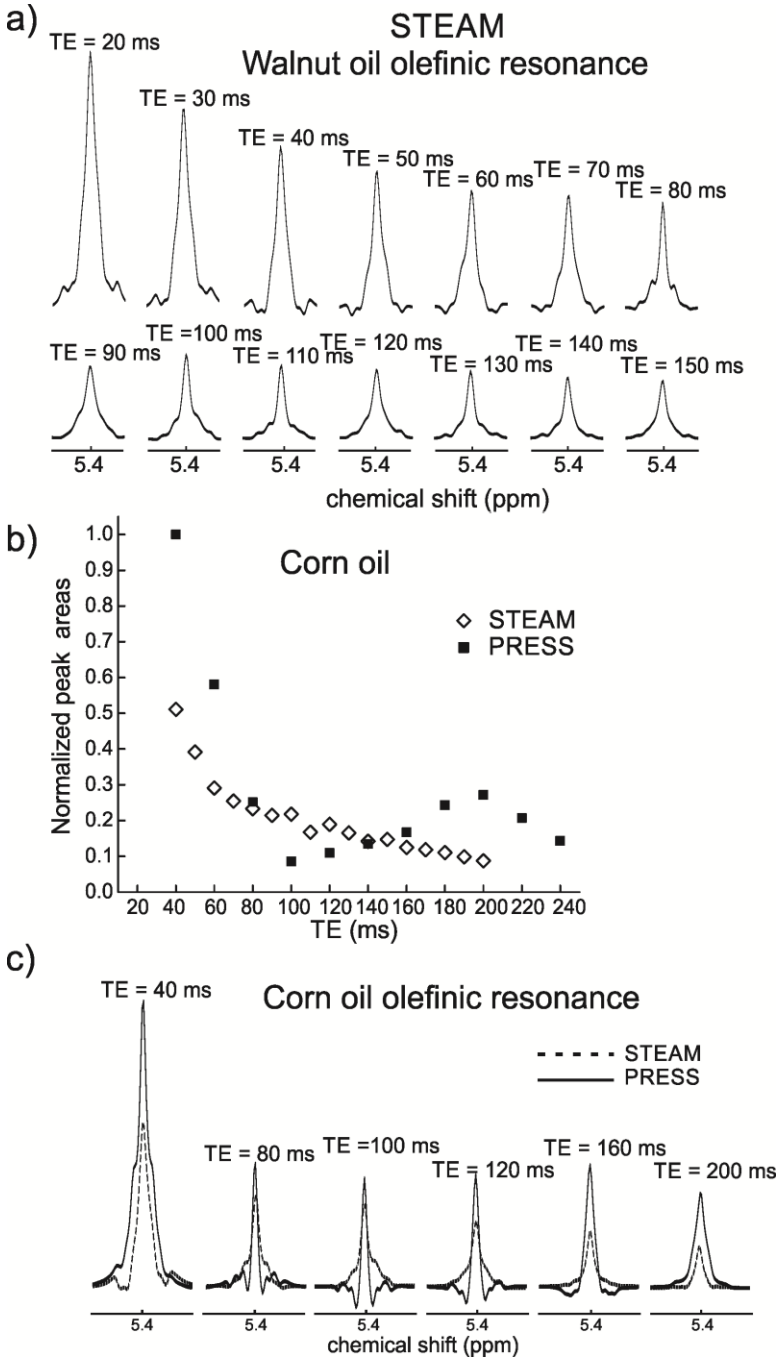

Figure 3.2. Walnut oil olefinic spectra as a function of STEAM TE (TM = 20 ms) are displayed in (a). The plots in (b) show corn oil olefinic peak areas in response to PRESS and STEAM. All areas are normalized to that obtained with PRESS TE = 40 ms. J-modulation effects are more clearly observed with PRESS. The bottom panel illustrates differences in corn oil olefinic spectral response to PRESS and STEAM for a few TE values. All peak heights are normalized to the maximum value obtained with PRESS (when TE = 40 ms).

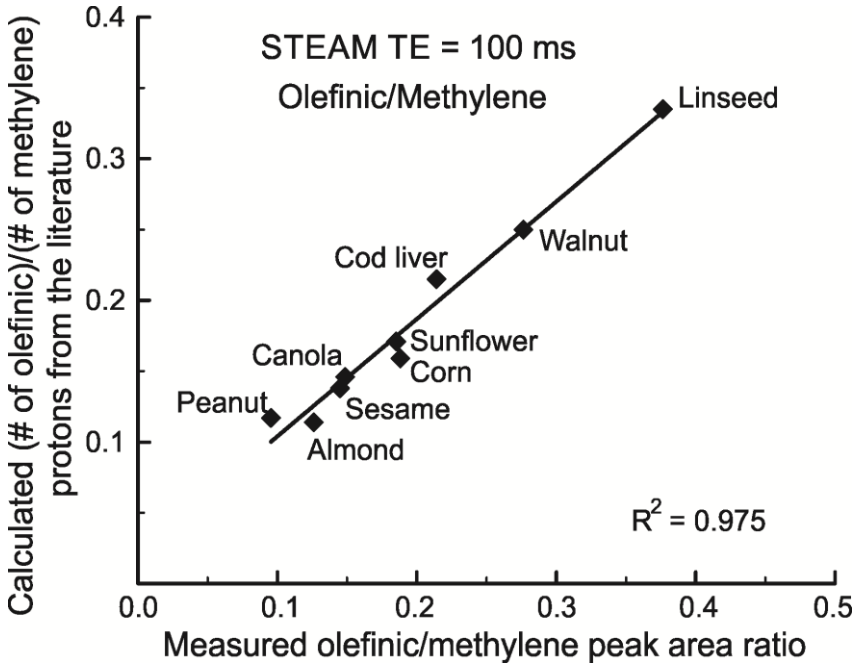

Figure 3.3. Mean olefinic/methylene ratios estimated from the literature for the nine oils[11] plotted against the olefinic/methylene peak area ratio obtained from the STEAM TE = 100 ms spectra (TM = 20 ms). A clear linear correlation is observed.

Figure 3.4 displays as an example the spectra obtained from the L4 vertebra of a normal volunteer. The overlap of water with the olefinic peak can be seen in the PRESS TE = 40 ms spectrum shown in Figure 3.4(a). Applying PRESS with a TE of 200 ms results in a well resolved olefinic peak as has been previously demonstrated; however, the STEAM TE = 100 ms sequence yields a well resolved olefinic peak that has 56% more area compared to the PRESS TE = 200 ms resonance. The improvement in signal is shown in Figure 3.4(b). The resulting signal enhancement by using the optimized STEAM sequence was 130%, 51% and 128% for the other three volunteers. The fitted olefinic and (methylene + methyl) peak areas were determined for each volunteer from the STEAM TE =100 ms, and PRESS TE = 200 ms spectra (fitted spectra are shown as dashed lines in Figure 3.4(a)). The ratio of the fitted olefinic peak area to that of the (methylene + methyl) peak was calculated for each volunteer for both the PRESS TE = 200 ms and STEAM TE = 100 ms spectra. The ratios obtained with STEAM were plotted against those obtained with PRESS for each volunteer and are shown in Figure 3.5. There is a clear linear correlation between the two ($R^2 = 0.972$).

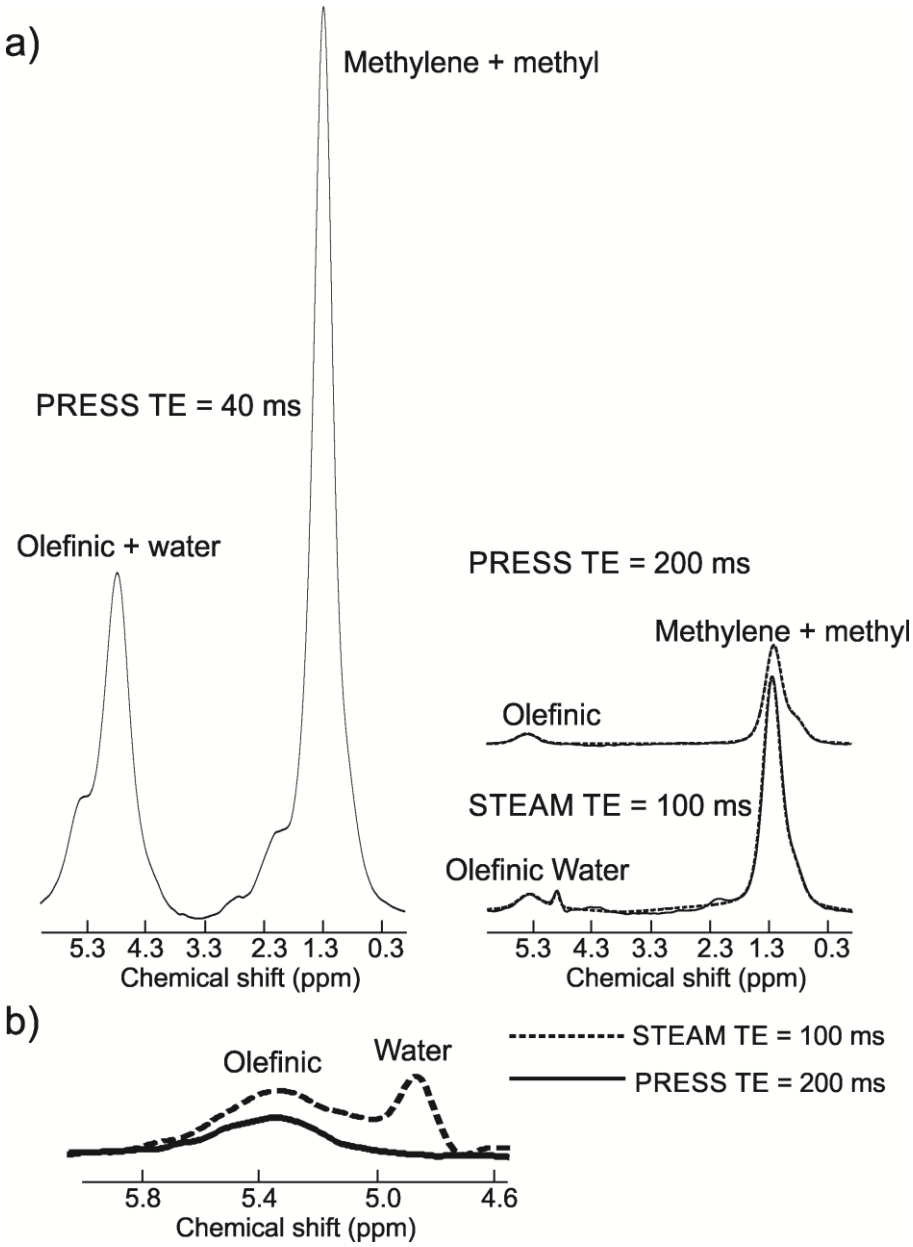

Figure 3.4. Panel (a) displays spectra measured from a voxel placed in the L4 vertebra of a healthy volunteer. The fitted spectra for the PRESS TE = 200 ms and STEAM TE = 100 ms are overlaid on the measured spectra as dashed lines. A residual water signal can be seen in the STEAM TE = 100 ms spectrum. Panel (b) shows the olefinic spectral region for the spectra obtained with the optimized PRESS and STEAM sequences. A significant enhancement in olefinic signal is observed with the TE = 100 ms STEAM sequence.

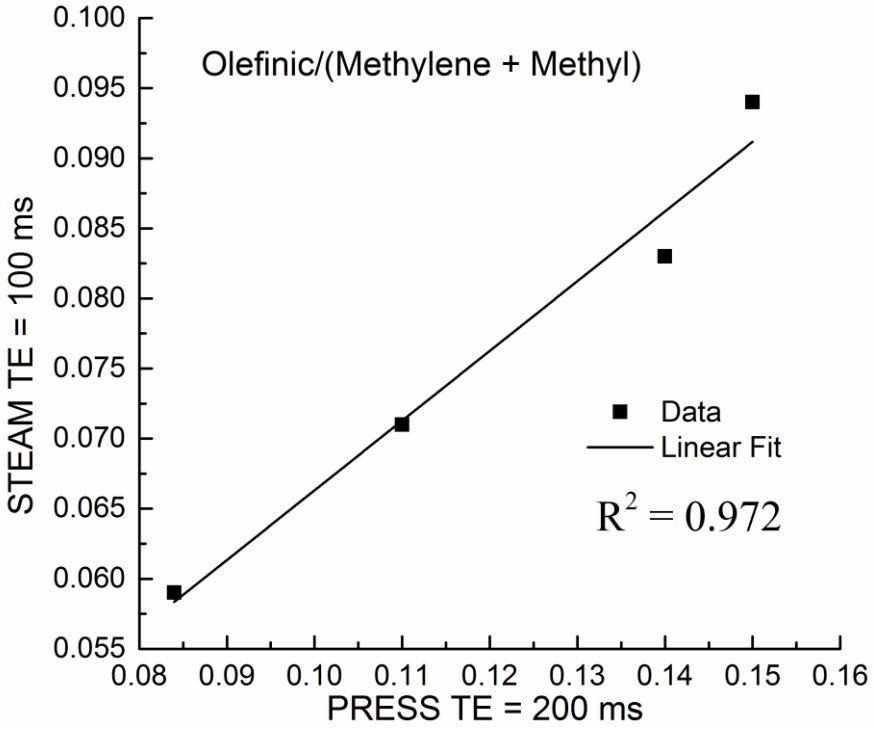

Figure 3.5. Olefinic/(Methylene + Methyl) peak area ratios calculated from STEAM TE = 100 ms and PRESS TE = 200 ms spectra for four volunteers. The ratios obtained from the STEAM spectra linearly correlate with those obtained from the PRESS spectra.

3.4 Discussion

The response of lipid olefinic protons to the STEAM pulse sequence was investigated in this work at 3 T. For long-TE values of 100 ms and higher, it was found that a mixing time of 20 ms yielded the highest olefinic signal area from the corn oil phantom. Employing a TM of 20 ms, the response of the olefinic protons as a function of STEAM TE was explored for all the nine oils. Small oscillations can be seen in Figure 3.1(b) and (c) which are believed to be due to chemical shift evolutions which take place during TM[18]. In the long TE vicinity the olefinic resonance exhibited maximum area for most oils when TE = 100 ms. The olefinic/methylene areas calculated for the oils from the STEAM TE = 100 ms correlated well with ratios deduced from oil compositions cited in the literature[11] as demonstrated in Figure 3.3 indicating that

STEAM with a TE of 100 ms is suitable for measuring relative levels of lipid unsaturation. While the nine edible oils listed above were employed in this investigation, it would be interesting to measure a few other edible oils too, such as olive, grapeseed, and avocado oil.

The response of corn oil olefinic protons to PRESS and STEAM (TM = 20 ms) were measured as a function of TE. As seen in Figure 3.2(b) J-modulation effects are more obvious in response to PRESS where a sinusoidal trend is visible unlike the response to STEAM where the only modulations observed are small oscillations, which are characteristic of the response of coupled spins to STEAM[18]. The phases of the side olefinic multiplets also vary with TE in response to PRESS whereas the multiplets all appear to be in phase for long TE values of STEAM. The relative olefinic signal yield from the optimized STEAM sequence (TM = 20 ms, TE = 100 ms) compared to that obtained with the previously optimized PRESS (TE = 200 ms) sequence was found to be 0.85 (on average from the nine oils). However, the olefinic signal yield was higher with the optimized STEAM sequence when applied *in-vivo* to spinal bone marrow. The olefinic signal area obtained with STEAM was a factor of 1.91 higher (averaged over the four volunteers) than the signal obtained with PRESS. The signal enhancement *in-vivo* is likely explained by the shorter T_2 values of the lipid olefinic protons *in-vivo* compared to that of the oils. The significantly shorter TE of the optimized STEAM sequence (100 ms as opposed to 200 ms for PRESS) reduces signal losses due to T_2 relaxation, thereby yielding a higher olefinic signal area compared to PRESS.

Previously it was shown that the optimized PRESS sequence yielded appropriate relative measures of the olefinic/(methyl + methylene) peak area ratios *in-vivo*[11] in spinal and tibial bone marrow. In this work, the olefinic/(methyl + methylene) peak area ratios were calculated for the spinal bone marrow of each volunteer from the STEAM TE = 100 ms and the PRESS TE = 200

ms spectra. As shown in Figure 3.5, the ratios obtained from the STEAM spectra highly correlate with those obtained with PRESS demonstrating that the optimized STEAM sequence yields relative measures of lipid unsaturation *in-vivo*.

In conclusion, we have demonstrated that an optimized STEAM sequence (TM = 20 ms, TE = 100 ms) can serve as an alternative to the previously optimized PRESS sequence (TE = 200 ms) for measuring relative levels of lipid unsaturation at 3 T and would be of particular advantage *in-vivo* in situations where SNR is a concern.

3.5 References

1. Q. He, P. Shkarin, R. J. Hooley, D. R. Lannin, J. C. Weinreb, V. I. J. Bossuyt. In vivo MR spectroscopic imaging of polyunsaturated fatty acids (PUFA) in healthy and cancerous breast tissues by selective multiple quantum coherence transfer (Sel-MQC): A preliminary study. Magnetic Resonance in Medicine **58**, 1079-1085 (2007).

2. M. A. Korteweg, W. B. Veldhuis, W. Th. M. Mali, S. C. E. Diepstraten, P. R. Luijten, M. A. A. J. van den Bosch, R. M. J. C. Eijkemans, P. J. van Diest, D. W. J. Klomp. Investigation of lipid composition of dissected sentinel lymph nodes of breast cancer patients by 7 T proton MR spectroscopy. Journal of Magnetic Resonance Imaging **35**, 387-392 (2012).

3. D. K. W. Yeung, J. F. Griffith, G. E. Antonio, F. K. H. Lee, J. Wood, and P. C. Leung. Osteoporosis is associated with increased marrow fat content and decreased marrow fat unsaturation: a proton MR spectroscopy study. Journal of Magnetic Resonance Imaging **22**, 279-285 (2005).

4. J. Machann, N. Stefan, C. Schabel, E. Schleicher, A. Fritsche, C. Würslin, H-U. Häring, C. D. Claussen, F. Schick. Fraction of unsaturated fatty acids in visceral adipose tissue (VAT) is lower in subjects with high total VAT volume - a combined ^{1}H MRS and volumetric MRI study in male subjects. NMR in Biomedicine **26**, 232-236 (2013).

5. N. A. Johnson, D. W. Walton, T. Sachinwalla, C. H. Thompson, K. Smith, P. A. Ruell, S. R. Stannard, J. George. Noninvasive assessment of hepatic lipid composition: Advancing understanding and management of fatty liver disorders. Hepatology **47,** 1513-1523 (2008).

6. P. Pollesello, O. Eriksson, K. Höckerstedt. Analysis of total lipid extracts from human liver by ^{13}C and ^{1}H Nuclear Magnetic Resonance Spectroscopy. Analytical Biochemistry **236,** 41-48 (1996).

7. P. A. Bottomley. Selective volume method for performing localized NMR spectroscopy. U.S. Patent 4,480,228 (1984).

8. J. Frahm, K-D. Merboldt, W. Hanicke. Localized proton spectroscopy using stimulated echoes. Journal of Magnetic Resonance **72**, 502-508 (1987).

9. J. Lundbom, S. Heikkinen, B. Fielding, A. Hakkarainen, M-R. Taskinen, N. Lundbom. PRESS echo time behavior of triglyceride resonance at 1.5 T: Detecting w-3 fatty acids in adipose tissue in vivo. Journal of Magnetic Resonance **201**, 39-47 (2009).

10. J. Lundbom, A. Hakkarainen, S. Soderlund, J. Westerbacka, N. Lundbom, M-R. Taskinen. Long-TE ^{1}H MRS suggests that liver fat is more saturated than subcutaneous and visceral fat. NMR in Biomedicine **24**, 238-245 (2011).

11. A. Troitskaia, B. G. Fallone, A. Yahya. Long echo time proton magnetic resonance spectroscopy for estimating relative measures of lipid unsaturation at 3 T. Journal of Magnetic Resonanace Imaging **37**, 944-949 (2013).

12. D. Burstein. Stimulated echoes: description, applications, practical hints. Concepts in Magnetic Resonance **8**, 269-278 (1996).

13. G. Hamilton, M. S. Middleton, M. Bydder, T. Yokoo, J. B. Schwimmer, Y. Kono, H. M.Patton, J. E. Lavine, and C. B. Sirlin. Effect of PRESS and STEAM sequences on magnetic resonance spectroscopic liver fat quantification. Journal of Magnetic Resonance Imaging **30**, 145-152 (2009).

14. J. M. Purcell, S. G. Morris, H. Susi. Proton magnetic resonance spectra of unsaturated fatty acids. Analytical Chemistry **38**, 588-592 (1966).

15. A. Barison, C. W. P. da Silva, F. R. Campos, F. Simonelli, C. A. Lenz, A. G. Ferreira. A simple methodology for the determination of fatty acid composition in edible oils through ^{1}H NMR spectroscopy. Magnetic Resonance in Chemistry **48**, 642-650 (2010).

16. K. Levenberg. A method for the solution of certain problems in least squares. Q Appl Math **2**, 164-168 (1944).

17. D. Marquardt. An algorithm for least-squares estimation of nonlinear parameters. SIAM J Appl Math **11**, 431-441 (1963).

18. R. A. DE Graaf, D. L. Rothman. In vivo detection and quantification of scalar coupled ^{1}H NMR resonances. Concepts in Magnetic Resonance **13**, 32-76 (2001).

Chapter 4 Concluding Remarks

In this thesis work, the response of lipid olefinic protons to the STEAM and PRESS sequences were investigated and compared at 3 T. PRESS and STEAM are the most commonly employed *in-vivo* MRS pulse sequences. The J-coupling signal evolution of the complicated olefinic proton spin system was measured as a function of PRESS and STEAM echo time, TE. Previous work determined that a PRESS sequence with a TE of 200 ms at 3 T almost completely suppressed the large water signal (in spinal bone marrow) that overwhelms the olefinic peak at shorter TE values. The optimal PRESS TE of 200 ms was selected because of the reduced signal loss due to J-coupling at that TE. The work in this thesis evaluated the response of the lipid olefinic protons to STEAM to determine: a) how the olefinic protons respond to long-TE STEAM, which to our knowledge has not been previously studied and b) whether a shorter optimal TE than 200 ms could be found with STEAM that sufficiently resolves the olefinic peak from water while minimizing signal losses due to J-coupling effects. A shorter TE reduces signal losses that result from T_2 relaxation.

The response of olefinic protons were examined for nine edible oils and the optimal STEAM parameters were found to be a mixing time, TM, of 20 ms and a TE of 100 ms. The *in-vitro* measurements showed that the response of the olefinic protons to STEAM was less intuitive than the response to PRESS, because of the dependence of signal on chemical shift differences between the coupled spins which causes rapid small oscillations in the signal. The optimized STEAM sequence yielded a well resolved olefinic peak from that of water *in-vivo* in spinal bone marrow. The optimized STEAM sequence provided from four volunteers on average a factor of 1.91 more olefinic signal compared to the previously optimized PRESS sequence.

The signal enhancement is due to less signal losses from T_2 relaxation with the shorter TE value. An enhancement of 91% is significant in MRS experiments where SNR is almost always a concern. STEAM would be advantageous in situations where levels of lipid unsaturation are low.

Future applications of the work involve measuring lipid unsaturation levels in breast tissue at 3 T.